scientific reports

Check for updates

OPEN

Assessment of structural stability and power performance for a novel hybrid wind-solar-wave energy system

Hongjian Zhang[1,2], Xiaodong Liu[2], Xinyu Cao[1], Ningchuan Zhang[1] &
Adrian Wing-Keung Law[3]✉

Integrated power generation systems have gained increasing attention in marine renewable energy development due to their potential synergistic benefits. However, quantitative assessments of the added gains in structural stability and power output are limited. This study proposes a novel wind-solar-wave (WSW) co-generation system that integrates wind, solar, and wave energy technologies to enhance both power performance per unit area and structural stability. A new numerical model is developed based on potential flow theory and multi-body hydrodynamic interactions, and validated using existing data. Eight WSW configurations are examined, considering varying mooring depths and clump weights. Results shows that the integration of wave energy converters (WECs) within and along the perimeter of WSW can improve the structural stability by reducing the vertical fluctuations of the floating solar farm by 41.2%-69.7% while contributing 11.3%-22.6% to the total power generated. Moreover, mooring the additional WECs and floating solar farms (FSFs) to the foundation of offshore wind turbines can also effectively control the overall structural motion of WECs and FSFs. Overall, the present study confirms the promising prospects of the WSW for future design and policy development of offshore energy integration, and also offer a new numerical model that can provide assessment and evaluation of the integrative benefits towards mooring structural stability and power performance for the whole system within the same spatial footprint.

Keywords Offshore wind turbine, Floating solar farm, Wave energy converter, Multi-body hydrodynamic, Mooring system

List of symbols
Acronyms

DOF	Degree of freedom
E&I	External and internal
FSF	Floating solar farm
HDPE	High-density polyethylene
JONSWAP	Joint north sea wave project
LC	Load case
LCOE	Levelized cost of energy
NREL	National renewable energy laboratory
O&M	Operation and maintenance
OB	Oscillating body
OWC	Oscillating water column
OWT	Offshore wind turbine
PTO	Power take-off
PV	Photovoltaic
RAO	Response amplitude operator

[1]State Key Laboratory of Coastal and Offshore Engineering, Dalian University of Technology, Dalian, China. [2]School of Civil and Environmental Engineering, Nanyang Technological University, Singapore, Singapore. [3]Department of Civil and Environmental Engineering, National University of Singapore, Singapore, Singapore. ✉email: cewklaw@nus.edu.sg

STD	Standard deviation
WEC	Wave energy converter
WSW	Wind-solar-wave co-generation system
Parameter	
B_{PTO}	PTO damping coefficient
d	Distance between upstream and downstream WECs
d_a	Asymptotic offset
$F_{k,\text{con}}$	Connector force matrix
$F_{k,\text{mooring}}$	Mooring cable force matrix
$F_{k,\text{PTO}}$	PTO force matrix
$F_{k,\text{wave}}$	Wave force matrix
Hs	Significant wave height
k_a	Asymptotic stiffness
K_{PTO}	PTO stiffness coefficient
L_0	Initial unstretched mooring length
M_{kj}	Inertial mass matrix
$P_{\text{downstream}}$	Power generation of downstream WECs
Pf	Probability of occurrence
P_{upstream}	Power generation of upstream WECs
P_{WEC}	Electricity generated by the WECs
TI	Turbulence intensity
Tp	Spectral peak period
x	Motion amplitude
φ_D	Diffraction wave potential
φ_I	Incidence wave potential
φ_R	Radiation wave potential
ξ_j	Motion acceleration
τ_{PTO}	PTO damping moment
θ_{arm}	Rotation angle of OB WEC
η_d	Linear decay rate of power generation per unit length
ω_{arm}	Rotation angular velocity of OB WEC

The advancement of marine renewable energies is crucial in the global energy transition towards decarbonisation which is urgently needed in order to meet the targets set by the Paris Agreement. Various marine renewable energy technologies, including offshore wind, wave, and solar, offer effective solutions to meet the energy demands while mitigating climate change impacts. Among these, offshore wind power has experienced the most rapid development in recent years and is now entering the commercialization phase. The forecast for global offshore wind turbine (OWT) installations indicates a projected growth to 36 GW by 2027, a substantial increase from 9 GW in 2022[1]. OWTs can be broadly categorized into two types based on their support structures: fixed OWTs and floating OWTs. Fixed OWTs are more suitable for countries with continental shelf coastlines, such as China, compared to floating OWTs. The related research on fixed OWTs has advanced significantly in various areas in recent years, including blade aerodynamics[2–5], dynamic response of wind turbines[6–9], structural integrity of foundations[10–13], and foundation scour[14–17]. In addition, offshore wind farms typically feature large spacing among the turbines to mitigate wake effects, leading to inefficient use of interior sea space.

The development of solar energy in coastal regions has also experienced rapid growth in recent years[18,19]. For example, China's solar power generation capacity reached 106 GW in 2022, representing 44% of the global installed capacity, with a cumulative capacity of 414.5 GW[20]. Water-based Solar Farms, benefiting from the cooling effect of seawater, can generate electricity more efficiently than their land-based counterparts[21]. The typical configurations of water-based solar farms include fixed solar farms, modular pontoon solar farms, very large floating structure solar farms and flexible floating structure solar farms. Among these floating options, modular pontoon solar farms are particularly economical and expandable. Therefore, the current mainstream solution for floating solar farm (FSF) is the modular pontoon solar farm. Currently, FSFs are more commonly deployed in reservoirs, lakes, and other calm water bodies so far[22–25]. Nonetheless, in the offshore environment, FSFs are exposed to wind, wave, and current, resulting in significant structural safety and life-span concerns.

Some research has been conducted on developing FSFs into the marine environment. Yang et al.[26] investigated the motion characteristics, the mooring tension, and the pressure on the photovoltaic (PV) panels of the FSF system under wave and wind loads. Research indicated that wave resonance may occur in FSFs under normal sea conditions, which could result in significant drifts and damage to the PV panels. Ma et al.[27] investigated the application of single-rod rigid connectors with varying degrees of freedom (DOFs) in floating PV systems, demonstrating through numerical simulations that connector type significantly affects float motion and load distribution. Magkouris et al.[28] performed a hydrodynamic analysis of FSF systems using the boundary element method to explore the impact of waves on FSF power generation under Mediterranean and Aegean Sea environmental conditions. The results demonstrated that the motion of the floating module alters the angle of sunlight incidence with the sea state, resulting in fluctuations in power generation. Sree et al.[29] employed experimental and numerical methods to evaluate the stress-strain and displacement of a modular FSF under wave action. The results showed that the interior of the FSF, away from the lateral mooring zone, exhibiting greater motion responses compared with its sides. On this basis, Zeng et al.[30] designed an adaptive barrier-mooring system for FSFs and explored the positioning ability of different mooring systems for FSFs under wave action based on experiments. The findings demonstrated that the innovative mooring system allows the FSF to accommodate up to a 36% change in water depth, while ensuring constant strain on the mooring cables.

Wave energy converters (WECs) have received a lot of attention in recent years. WECs can be classified as follows[31]: oscillating body (OB) WECs, oscillating water column (OWC) WECs, and overtopping WECs. OB WECs have garnered significant attention due to their affordability and suitability for modular installation. Research by Castro-Santos et al.[32] indicated that the economic efficiency of wave energy farm alone is lower compared to other offshore renewable energies. Hence, WECs are more often used as anti-wave devices for various offshore structures, e.g., offshore wind power[33–36], very large floating structures[37–40], breakwaters[41–44].

In recent decades, there has been a growing trend of reducing Levelized Cost of Energy (LCOE) by integrating various renewable energy conversion systems into hybrid power system[33] such that the power output can be increased within the same special footprint. Various conceptual schemes have been proposed for these integrated offshore energy systems in the literature, including wind-wave co-generation[33–36], wind-tidal co-generation[45,46], and wave-tidal co-generation[47–50]. For example, the issue of unused sea surface space in offshore wind farms can be alleviated by deploying offshore solar farms among the OWTs. This is similar to onshore wind farms which install solar farms on unused land among the wind turbines, which increases the total power generation while reducing the intermittency issue of renewable energy generating units[51–53]. Similarly, WECs can potentially be installed in a meshed configuration both around and within the modular FSF, dissipating wave energy and enhancing total power generation at the same time. Jariwala et al.[54] investigated a hybrid solar-wind-wave energy converter that combines PV panels and a vertical-axis wind turbine on a point absorber WEC. Their study emphasized control strategies for power conversion under emulated real-sea conditions based on a single integrated floating structure rather than a modular system.

This study proposes a novel concept for an offshore wind-solar-wave (WSW) co-generation system that synergistically integrates wind, solar, and wave energy to increase the power output per unit area of the permitted site. The concept integrates the modular FSFs and WECs between OWTs in order to maximize the use of available spatial footprint. Furthermore, the new configuration secures the mooring system of the FSFs to the fixed foundations of the OWTs, eliminating the need for complex anchoring, and the WEC arrays are deployed along the FSF perimeter to reduce wave impact while enhancing overall power generation. Additionally, interior WECs are designed as Power-Take-Off (PTO) systems which can act as the internal connectors between FSF modules, leveraging their relative motion to improve both structural stability and energy production. Previous studies have explored offshore multi-energy concepts, ranging from co-located wind-solar-wave parks sharing transmission infrastructure[54] to fully hybrid systems that integrate all three energy converters into a single floating unit[55]. In contrast, the present work proposes a new concept of semi-integrated systems in which WECs are structurally meshed with FSF systems, while OWTs simultaneously provide the power generation and mooring functionality. The semi-integration distinguishes our design from both co-located and fully hybrid approaches that have been suggested in the literature so far. A new numerical model for the WSW co-generation system is also developed to comprehensively analyze the dynamic response and power generation of various WSW configurations, as well as the influence of anchor depth and clump weight on the system motion. The findings provide valuable design insights on improved structural stability and increased power performance for future WSW development, offering a theoretical foundation and technical guidance for the integrated utilization of offshore renewable energy resources.

The structure of this paper is as follows. Section 2 introduces the WSW concept. Section 3 presents the development of the numerical model, followed by Section 4, which details the validation of the model. Section 5 investigates the structural stabilities of the WSW system, while Section 6 analyses the power output performance. Finally, Section 7 summarizes the key findings and provides conclusions.

Concept of wind-solar-wave co-generation system

Figure 1 illustrates the schematic diagram for the proposed WSW co-generation system concept which comprises three components: monopile OWTs, FSFs, and WECs. The WSW layout with its mooring system is also shown in the figure.

Currently, OWTs are typically spaced 5–7.5 times the rotor diameter[56,57] (i.e. the spacing is approximately 600–1000 m) to mitigate wake effects, leaving large areas of unused sea space in practice. Installing FSFs in these open areas can optimize the space utilization while enabling shared electrical inverters and cabling. At the same time, OWTs are generally located in offshore regions with strong wind conditions to maximize the power generation, and thus FSFs may experience significant structural displacements with their extensive spatial extent of photovoltaic (PV) module. To mitigate the wave-induced platform motion while enhancing the energy production, WECs are strategically integrated both along the perimeter and within the FSF, simultaneously sharing electrical components to improve overall techno-economic performance.

The WEC design follows a mesh approach. External WECs are attached to the FSF's perimeter modules, with PTO devices converting the relative motion between WECs and perimeter modules into electricity. Additionally, internal WECs are formed by integrating PTO devices into the FSF's internal connectors, utilizing the relative motion between adjacent modules for additional power generation.

Additionally, the OWTs' fixed foundations serve as part of the FSF mooring system, reducing anchoring costs. The mooring system is secured at the top to the FSF's perimeter modules, while the bottom end is anchored either to the seabed or to the OWT foundations, depending on site conditions. Mooring cables are typically fitted with clump weights to counteract the reduced positioning stability caused by tidal variations.

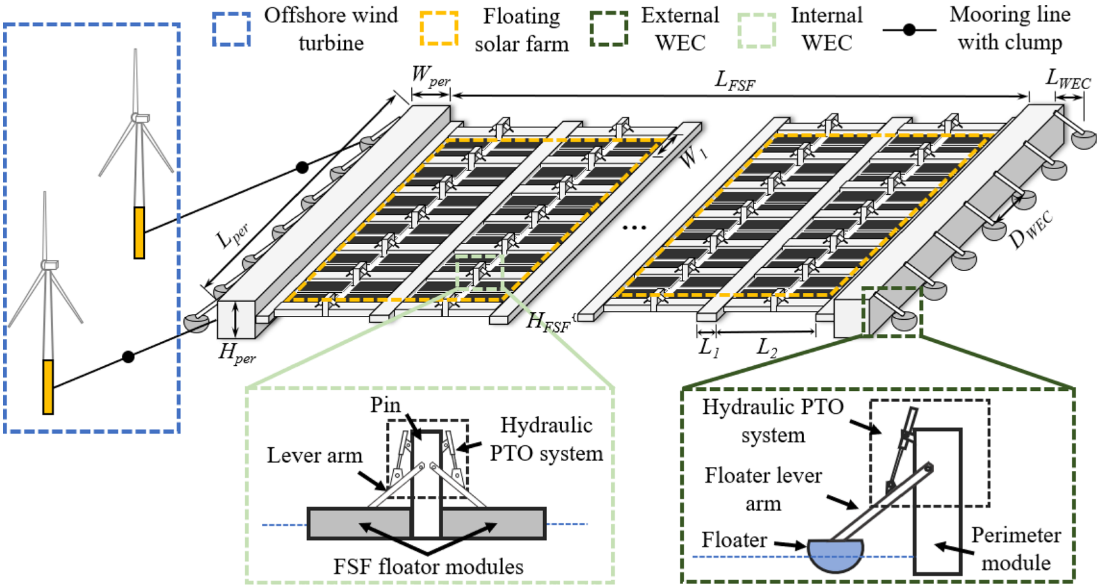

Fig. 1. Schematic diagram of wind-solar-wave (WSW) co-generation system.

Numerical model

We utilize a numerical model in this study to quantify the benefits that can be generated from one application instance derived from the proposed concept. The model, based on the commercial software ANSYS AQWA (version 2018)[58], employs potential flow theory to analyses the flow field surrounding the floating bodies, including the FSF modules and attached WECs, as well as the hydrodynamic interactions among them. It incorporates both radiation coupling and shielding effects. Accounting for these interactions alters both the radiation and diffraction wave forces, leading to variations in the hydrodynamic response. Consequently, the response amplitude operator (RAO) for each structure differs from that obtained when the structures are considered in isolation.

To account for the hydrodynamic interactions among multiple structures, the total DOFs needed would be 6×m, with m representing the number of structures. The overall unsteady potential can be obtained through superposition,

$$\varphi\left(\vec{X}\right) = \varphi_I + \varphi_D + \sum_{m=1}^{m}\sum_{j=1}^{6}\varphi_{Rjm}x_{jm} \tag{1}$$

where φ_I represents the incident wave potential, φ_D the diffraction wave potential, φ_{jm} the amplitude of motion of the jth DOF of the mth structure. φ_{Rjm} denotes the radiation wave potential due to the jth DOF of the mth structure, while other structures remain stationary. The incident wave potential is computed using the linear wave theory, while the diffraction and radiation wave potentials are determined through the source distribution method. Following the computation of the unsteady potentials, the wave excitation force acting on the wet surface of each structure is obtained through integration.

The numerical model considers the FSF and perimeter WECs in the proposed WSW concept as the main structure, while the internal WECs and OWTs are simplified as connectors and part of mooring system, respectively. In the hydrodynamic simulations, the OWTs were treated only as mooring points without considering aerodynamic loads on the WSW system, while their power generation was estimated separately using the wind speed-power curve. The PV panels were represented as an integral part of the FSF structure, and their output was assumed constant under normal operating conditions, following Bi et al.[59]. Large scale FSFs typically comprise numerous floating modules numbering in millions, with a significantly larger horizontal dimension compared to the vertical dimension, resulting in evident flexible characteristics[29]. In the present study, the PV modules are interconnected with numerous WECs, thereby forming a fully integrated multi-float configuration. It is too computationally expensive to simultaneously solve the flexible structural characteristics of FSF and the full-scale multi-body hydrodynamic interactions with WECs in the numerical simulations. Therefore, the WSW system is simplified as multiple rigid floats (i.e., external WEC and PV modules), which are interconnected with joints (i.e., internal WEC), and moored to the bottom (i.e., seabed or the foundation of OWT). The numerical model is meshed using a maximum element size of 1 m, with the FSF module element size of 0.4 m, WEC element size of 0.3 m, and a defeaturing tolerance of 0.05 m. A total of 27,848 elements are established, of which 14,190 are diffraction elements.

The connector and PTO models in this study operate under two assumptions[60]. First, the relative displacements between neighbouring floats are disregarded, and the analysis focuses solely on relative rotations. Second, the connector and PTO models are simplified as joint models with linear stiffness and damping characteristics.

Figure 2 illustrates the simplified connector model and the PTO model. The connectors are modelled with rotational stiffness around the Y direction, and linear damping is incorporated to simulate the PTO systems with internal WECs. In the absence of internal WECs, the damping for the connector model is set to 0. The PTO systems for external WECs are treated as linear spring-damping systems, which convert the relative motion of the floats into electricity. The damping moment for PTO systems are expressed as

$$\tau_{PTO} = B_{PTO} \cdot \omega_{arm} + K_{PTO} \cdot \theta_{arm} \tag{2}$$

where B_{PTO} is the PTO damping coefficient, K_{PTO} the PTO stiffness coefficient, τ_{PTO} the PTO damping moment, ω_{arm} the angular velocity of float relative rotation, and θ_{arm} the relative rotation angle. The electricity P_{WEC} generated by the WECs is expressed as

$$P_{WEC} = \tau_{PTO} \cdot \omega_{arm} \tag{3}$$

The WSW's mooring cable is modelled as a nonlinear steel wire rope with its weight being neglected. Its tension is expressed as follows:

$$T = \begin{cases} k_a \left(L - L_t\right) \; if \; L > L_t \\ 0 \; if \; L \leq L_t \end{cases} \tag{4}$$

where $L = \left|\overrightarrow{X}_1(t) - \overrightarrow{X}_2(t)\right|$ and $L_t = L_0 + d_a \tanh\left((L - L_0)/d_a\right)$. k_a denotes the asymptotic stiffness, d_a the asymptotic offset, L_0 the initial unstretched mooring length, $\overrightarrow{X}_1(t)$ and $\overrightarrow{X}_2(t)$ are the attachment points on the structures and seabed.

Considering the multi-body hydrodynamic interactions with the connector effects, the motion equations for the *k*th structure (*k* = 1, 2, …, *m*, where *m* is the total number of floating structures in the WSW system) can be expressed as,

$$\sum_{j=1}^{6m} \left[(M_{kj} + A_{kj}(\omega))\, \ddot{\xi}_j(t) + B_{kj}(\omega)\dot{\xi}_j(t) + C_{kj}(\omega)\xi_j(t)\right] = F_{k,wave}(t) + F_{k,con}(t) + F_{k,PTO}(t) + F_{k,mooring}(t) \tag{5}$$

where $\ddot{\xi}_j, \dot{\xi}_j, \xi_j$ denote the motion acceleration, velocity and displacement of the *j*th DOF, respectively; M_{kj} is the mass matrix; $A_{kj}(\omega), B_{kj}(\omega), C_{kj}(\omega)$ are the added mass matrix, radiation damping matrix, and hydrostatic restoring, respectively; ω is the wave angular frequency; $F_{k,wave}$ is the wave-induced force matrix, including the hydrostatic restoring force matrix, radiation force matrix and excitation force matrix; $F_{k,con}$ is the connector force matrix; $F_{k,PTO}$ is the PTO force matrix; and $F_{k,mooring}$ is the mooring cable force matrix. It should be noted that the viscous force is not considered in this model. The set of equations was solved in the time domain using the built-in solver of ANSYS AQWA with a fixed time step of 0.003 s.

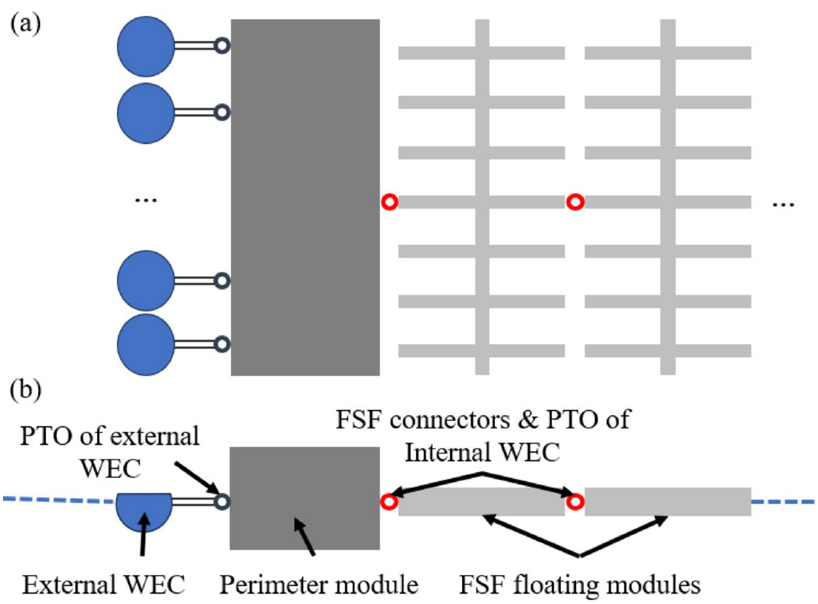

Fig. 2. Schematic diagram of FSF connectors and WEC PTO system: (**a**) Top view, and (**b**) Side view.

Validation

Validation of FSF

To ensure the reliability of the simulations, the numerical model implemented in ANSYS AQWA was validated against the experimental data reported by Zeng et al.[30], which focused on the motion responses of the FSF system under wave excitation. Figure 3 presents the schematic diagram of the experimental setup. The wave flume dimensions were 35 m length, 0.55 m width, and 0.6 m depth. The flume was equipped with grid-type wave attenuators at both ends, with a downstream beach slope of 1:13 to minimize wave reflection effects. The FSF model was made with a scale of 1:30 based on the Froude similarity, and employed a floating perforated plate made of ethylene vinyl acetate foam with an equivalent stiffness equal to the shell structure of the prototype. The distance between the FSF model and the wavemaker was 12.5 m. A linear spring, with a model stiffness of 2.5 N/mm and a pretension of 1.4 N, was utilized to simulate the elasticity of the actual steel wire rope. The anchoring system was fixed to the flume bottom using steel plates. The experiment was conducted under regular wave conditions, with a prototype wave height of 0.3 m and a prototype wave period of 2.2 s, 2.9 s, 3.4 s, and 4.1 s, and the field water depth was 10.8 m.

Figure 4 presents the horizontal and vertical displacement distributions of the FSF model, comparing experimental results with numerical predictions for regular waves. In all cases, the numerical predictions successfully capture the overall magnitude and spatial variation trends observed in the experiments. The mean horizontal displacement shows close agreement with the experimental results, with deviations generally within 10% across the tested cases. The vertical displacement predictions also agree well with the measurements, although discrepancies increase slightly with wave period. Nonetheless, the overall variation patterns remain consistent.

Validation of WEC

The calculated motion responses were compared with the experimental data of a 1:5 scale Wavestar prototype tested by Windt et al.[61], to further assess the accuracy of the numerical model for simulating WECs in this study. The experiments were carried out under regular wave conditions with the wave height of 0.1 m and wave period of 1.4 s. Figure 5 compares the simulated heave motions with the experimental measurements under different PTO damping coefficients, the amplitude deviations typically within 5–10%, which demonstrates good agreement between them. Some discrepancies were observed in the peak responses under high damping conditions, which can be attributed to fact that the simplified linear damping model of the PTO system in the numerical method does not include potential nonlinear mechanical behaviours and hysteresis effects. Nevertheless, the validation confirms that the model can reasonably reproduce the motion responses of individual WECs. It should be noted that this validation was carried out for a single WEC rather than the fully integrated multi-body system. Hence, potential hydrodynamic coupling effects between modules are not directly verified. Nevertheless, the numerical methods employed in this study demonstrate acceptable accuracy and reliability within this limitation.

Structural stabilities

The structural stability of the novel WSW is investigated by considering different configurations under various sea states in this section. The dynamic response of various combinations of WECs and FSFs are first examined to ascertain an optimal configuration with the objective of minimizing motion response. Subsequently, the impacts of mooring anchor depth and clump weight on the dynamic response for WSW are investigated to identify a suitable mooring solution.

Description of the WSW configurations

Typical sea state conditions considered for National Renewable Energy Laboratory (NREL) 5 MW OWT are adopted in this study as shown in Table 1, which includes the water depth, turbulence intensity (*TI*), significant wave height (*Hs*), spectral peak period (*Tp*), and probability of occurrence (*Pf*). These parameters are obtained from measurements conducted at the IJmuiden Munitiesstort site[62,63]. The irregular waves follow the JONSWAP spectrum with a spectral peak factor of 3.3.

The details for the three key renewable energy devices (wind, solar and wave) of the WSW are summarized in Table 2. The OWT is considered as a shared mooring foundation[64]. Additionally, the FSF measures 16.5 m in width and 63 m in length, comprising a total array width of 13 modules and a length of 50 modules. Each float module, made of high-density polyethylene (HDPE) with a Young's modulus of 500 MPa, is hollow and measures 1.26 m in length, 0.4 m in width, 0.215 m in height, and 3 mm in thickness[30]. Perimeter pontoons are installed around the FSF to provide buoyancy and wave resistance. Furthermore, the Wavestar concept[65]

Fig. 3. Experimental setup (from)[30].

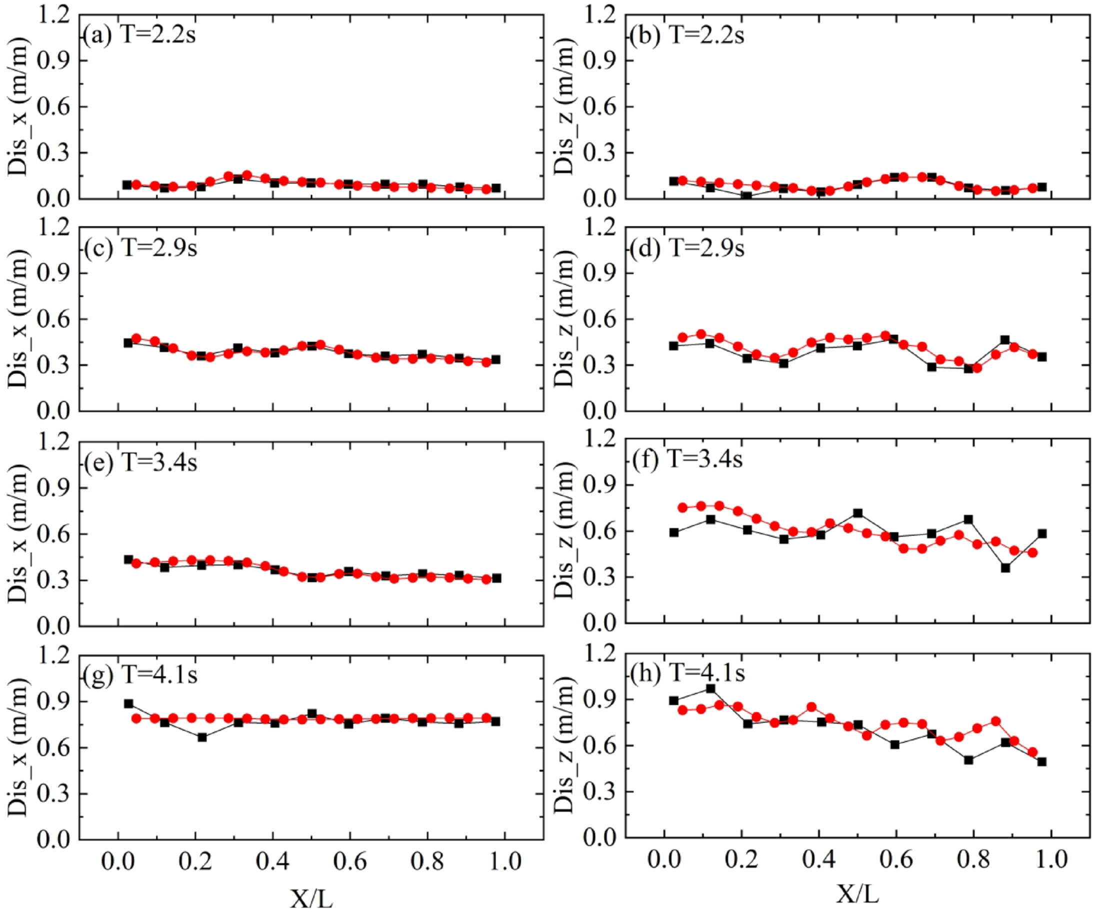

Fig. 4. Validation of the numerical model against experimental results[30] for the displacement of the FSF in the X (left column) and Z (right column) directions: (**a**, **b**) T = 2.2 s, (**c**, **d**) T = 2.9 s, (**e**, **f**) T = 3.4 s, and (**g**, **h**) T = 4.1 s. Legend: black line with squares = experimental results, red line with circles = numerical model.

is used for the external WEC employed together with perimeter pontoons as protection against waves. The Wavestar WEC comprises a hemispherical float and a steel arm. The motion of float drives the rotation of the steel arm, which in turn compresses the hydraulic PTO system to generate electricity. For the FSF, adjacent floating modules are connected with Nylon pins supporting the PV panels on top. Similar PTO devices are installed in the connections to form internal WECs, utilizing the mechanical energy due to the relative motion of adjacent floating modules. Finally, mooring cables and anchoring system regulate the motion response of the entire system.

The validated numerical model is adopted by building a two-dimensional numerical setup and installing the WECs in the direction of wave propagation to examine the dynamic response of the WSW concept. Figure 6 presents a schematic of the WSW farm and three combinations of WECs and FSF. The combinations of WECs and FSF can be categorized as follows:

(1) External WECs + FSF: OB WECs are installed on the perimeter modules of the FSF, which can help dampen waves propagating into downstream FSF modules. The relative motion between the WECs and perimeter modules due to the phase difference of waves drives the PTO devices, as illustrated in Fig. 6a.
(2) Internal WECs + FSF: PTO devices are installed on the FSF's internal connectors between the adjacent FSF modules. The relative motion of the adjacent FSF modules drives the PTO devices, thus creating the power production, as illustrated in Fig. 6b.
(3) E&I WECs + FSF: The external and internal PTO devices are both installed within the FSF, as illustrated in Fig. 6c.

Table 3 outlines various configurations of WECs and FSF. To explore the effect of asymmetrical installations of WECs on FSF, with the configurations of WECs on either front or rear side of FSF are investigated, respectively. Con 1 denotes a single FSF without WECs. Cons 2–4 indicate WECs installed solely at the perimeter of the FSF, with EF and ER denoting external WECs installed on the front and rear sides of the FSF, respectively. Con 5 signifies WECs installed within the FSF. Cons 6–8 involve both external and internal WECs located within the FSF.

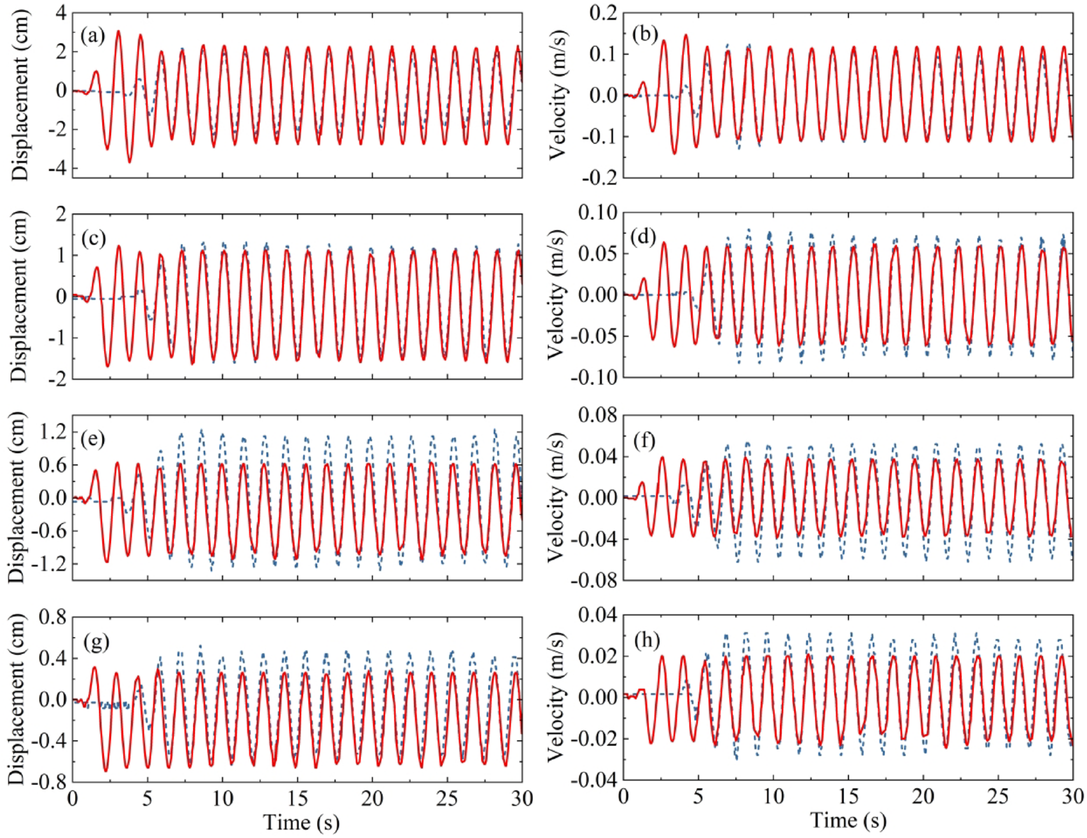

Fig. 5. Comparison of Wavestar WEC responses under different damping coefficients: (**a**, **b**) 0 N·m·s; (**c**, **d**) 50 N·m·s; (**e**, **f**) 100 N·m·s; (**g**, **h**) 200 N·m·s, where (**a**, **c**, **e**, **g**) show displacement and (**b**, **d**, **f**, **h**) show velocity. Legend: blue dashed line = experimental results, red solid line = numerical model.

Load cases	Wind		Wave		
	V (m/s)	*TI*	*Hs* (m)	*Tp* (s)	*Pf* (%)
1	12	14.6	1.67	5.89	14.582
2	16	13.9	2.16	6.34	8.216
3	20	13.4	2.71	6.96	3.48

Table 1. Design load cases.

Dynamic response

Figure 7 illustrates the horizontal and vertical motion of the FSF for different configurations with LC1. Compared to the FSF without WECs, those with external WECs show varying decrease in maximum vertical displacement but generally exhibit increased maximum horizontal displacement. This is because the external WECs are exposed to higher horizontal wave forces due to larger cross sections, whereas the conversion of energy dampens the waves and shelters the downstream FSF modules. Installing only internal WECs reduces the maximum vertical displacement of the FSF by up to 63.6%, subsequently decreasing the maximum horizontal displacement by up to 22.9%. The difference in motion response between configurations with and without internal WECs is negligible when external WECs are already installed, indicating that the external WECs provide the dominate wave-sheltering effects. However, internal WECs reduce the standard deviation (STD) of the vertical displacement of the FSF's internal floats. This reduction becomes more pronounced with increased motion of the floating body. As the FSF's scale expands to the hundred-meter level or larger, the wave-sheltering effects of external WECs possibly decreases, so the installation of internal WECs can enhance structural safety by mitigating the extreme vertical displacements of the FSF's internal floats. Installing WECs on the rear side of the FSF is less effective in wave sheltering and leads to a 60.4% increase in maximum horizontal displacement compared with the case of the FSF with internal WECs only, as the upstream modules dissipate most of the high-frequency wave energy, leaving low-frequency components to excite the rear WECs, while hydrodynamic coupling among multiple bodies further amplifies the low-frequency surge response. Moreover, installing external WECs on the rear side causes more pronounced vertical motion fluctuations compared to those with

Properties		Value	Unit
Offshore wind turbine			
Wind turbine rated power		5	MW
Cut-in/rated/cut-out wind speed		3/11.4/25	m/s
Rotor diameter		126	m
Tower height		77.6	m
Monopile height		30	m
Monopile diameter		6	m
Water depth		20	m
Floating solar farm			
Length of perimeter module L_{per}		16.5	m
Width of perimeter module W_{per}		2.1	m
Height of perimeter module H_{per}		1.5	m
Length of FSF L_{FSF}		63	m
Height of FSF H_{FSF}		0.215	m
Width of the module supporting PV panel L_1		0.4	m
Width of the module supporting PV panel L_2&W_1		2.58/2.12	m
Stiffness coefficients of connectors		50	kN/m
Diameter of steel wire rope		0.038	m
Axial stiffness of steel wire rope		2250	kN/m
Pre-tension of steel wire rope		37.8	kN
Length of the mooring cable		39.33	m
Angle between mooring cable and horizontal plane		30	deg
External/Internal wave energy converter			
Mass of external WEC		3437.5	kg
Mass moment of inertia of external WEC		121,289	kg·m^2
Centre of mass (CoM) of the of external WEC relative to the hinge position	X	3.488	m
	Y	0	m
	Z	−3.3265	m
Draft of external WEC		1	m
Distance between external WECs D_{WEC}		2.52	m
Distance between external WEC and perimeter module L_{WEC}		1.5	m
Damping coefficient of external WEC		2	kN/m·s
Damping coefficient of internal WEC		2	kN/m·s
Stiffness coefficient of external WEC		2	kN/m
Stiffness coefficient of internal WEC		0	kN/m

Table 2. Parameters of the combined concept system used in the present analysis.

WECs mounted at the front. However, symmetrical WEC installation stabilizes the FSF in its initial position, reducing both the maximum and the STD of vertical motion.

Figures 8 and 9 depict the horizontal and vertical motions of the FSF for different configurations with LC2 and LC3. Similar to observations at LC1, installing external WECs symmetrically at both ends of the FSF reduces the vertical motion of the internal floats and mitigates the horizontal displacement. Motion responses between configurations with and without internal WECs show insignificant differences when external WECs are absent. The enhancement of structural safety by installing only internal WECs within the FSF diminishes with LC2 and LC3. Internal WECs suppress local vertical motion by controlling the relative rotation between FSF modules. However, since the wavelength is close to or more than the length of the FSF with LC2 and LC3, the relative rotation angle between the modules decreases.

Figure 10 presents the horizontal displacement time history curves and motion spectra of the WSW under LC3 with and without internal and external WECs. The results show that incorporating WECs could reduce vertical motion, while the installation of external WECs leads to an additional increase in horizontal displacement amplitude, with the maxima rising by approximately 49.3% compared with the baseline FSF. This enlarged motion implies that wider safety gaps may be required in practical deployments and that the mooring lines and connectors could be subjected to higher dynamic loads. Additionally, the motion spectra indicates that WECs perform effectively in suppressing high-frequency responses. Nevertheless, external WECs tend to introduce multi-body interactions and resonance effects associated with the WEC itself. These findings highlight the trade-off between enhanced energy capture and increased structural drifts, underlining the need for optimized WEC placement in future engineering applications.

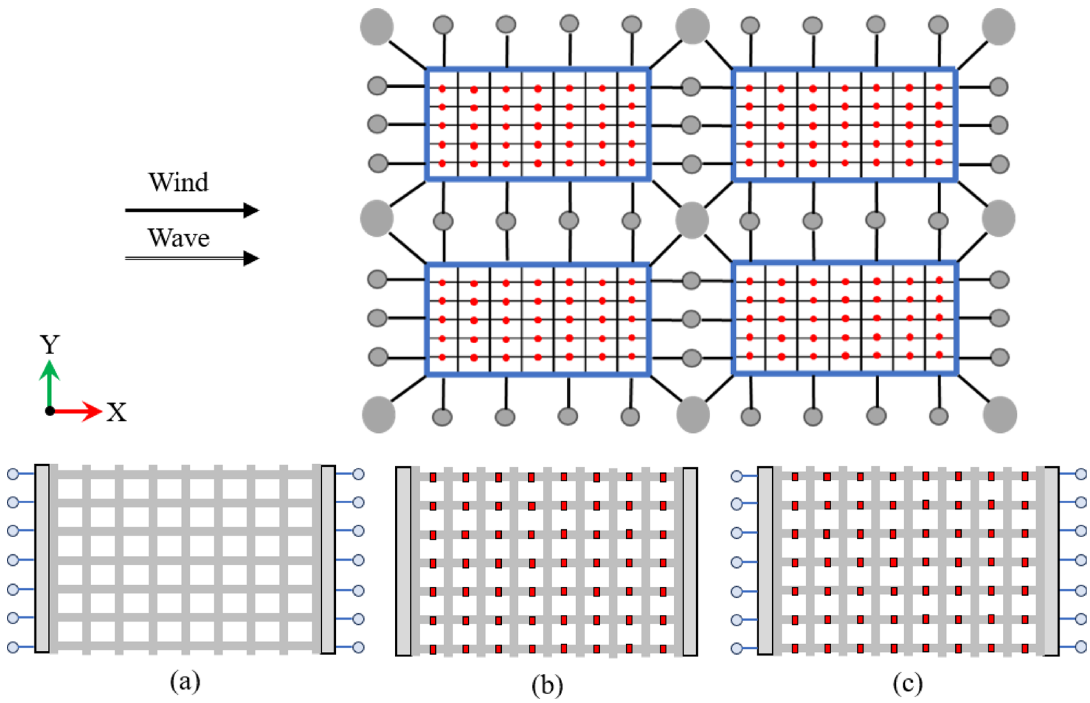

Fig. 6. Layout of offshore WSW co-generation system. Top: Schematic diagram of offshore WSW farms. Legend: grids = floating solar system, large gray circles = fixed-bottom OWTs, little gray circles = fixed foundation, blue lines = external WECs, red circles = internal WECs, black lines = mooring lines. Bottom: (**a**) external, (**b**) internal and (**c**) both external and internal WECs combined with FSF.

Configuration	WSW definition	External WEC installed at the front of the FSF	External WEC installed at the rear of the FSF	Internal WEC
1	Single FSF	No	No	No
2	EF_WEC + FSF	Yes	No	No
3	ER_WEC + FSF	No	Yes	No
4	E_WEC + FSF	Yes	Yes	No
5	I_WEC + FSF	No	No	Yes
6	EF/I_WEC + FSF	Yes	No	Yes
7	ER/I_WEC + FSF	No	Yes	Yes
8	E/I_WEC + FSF	Yes	Yes	Yes

Table 3. Definitions for different WSWs.

Figure 11 illustrates the mooring tension for different WSW configurations of the three LCs. Cables 1 and 4 indicate the mooring cables on the incident side, while cables 2 and 3 indicate the cables on the rear side. The figures show that the maximum and mean mooring tension of the FSF equipped with internal WECs are significantly smaller than those of the other configurations. This is because the installation of internal WECs reduces the relative motion between adjacent modules within the FSF, reducing the displacement of both ends moving toward the centre of the FSF and thus decreasing the mooring tensions. In rough sea conditions (LC2 and LC3), both the maximum and mean mooring tensions for the FSF with WECs are lower compared to those for the FSF without WECs. Symmetrically installed WECs provide greater stability for FSFs compared to unilaterally installed WECs. This reduction is attributed to the decreased motion response, enhancing the mooring system.

Figure 12 illustrates the joint loads of the FSF's connectors for different configurations with LC1. The mean horizontal force (Fx) at the joints of the FSF with internal WECs are around 10% lower than the single FSF due to the smaller relative rotation of joints between adjacent FSF modules, while the rotational torque in the Y direction at both ends are 30% lower. Regarding the external WECs, the configurations with installations on the incident side efficiently reduce both the magnitude and fluctuation of the joint force in the x-axis (Fx) on the FSF. The configurations with WECs installed on the rear side or both ends of the FSF exhibit a slightly higher mean value of Fx compared to other configurations.

Figures 13 and 14 illustrate the joint loads of the FSF's connectors for different configurations with LC2 and LC3. The installation of WEC in FSFs can significantly decrease the joint loads with moderate or severe sea

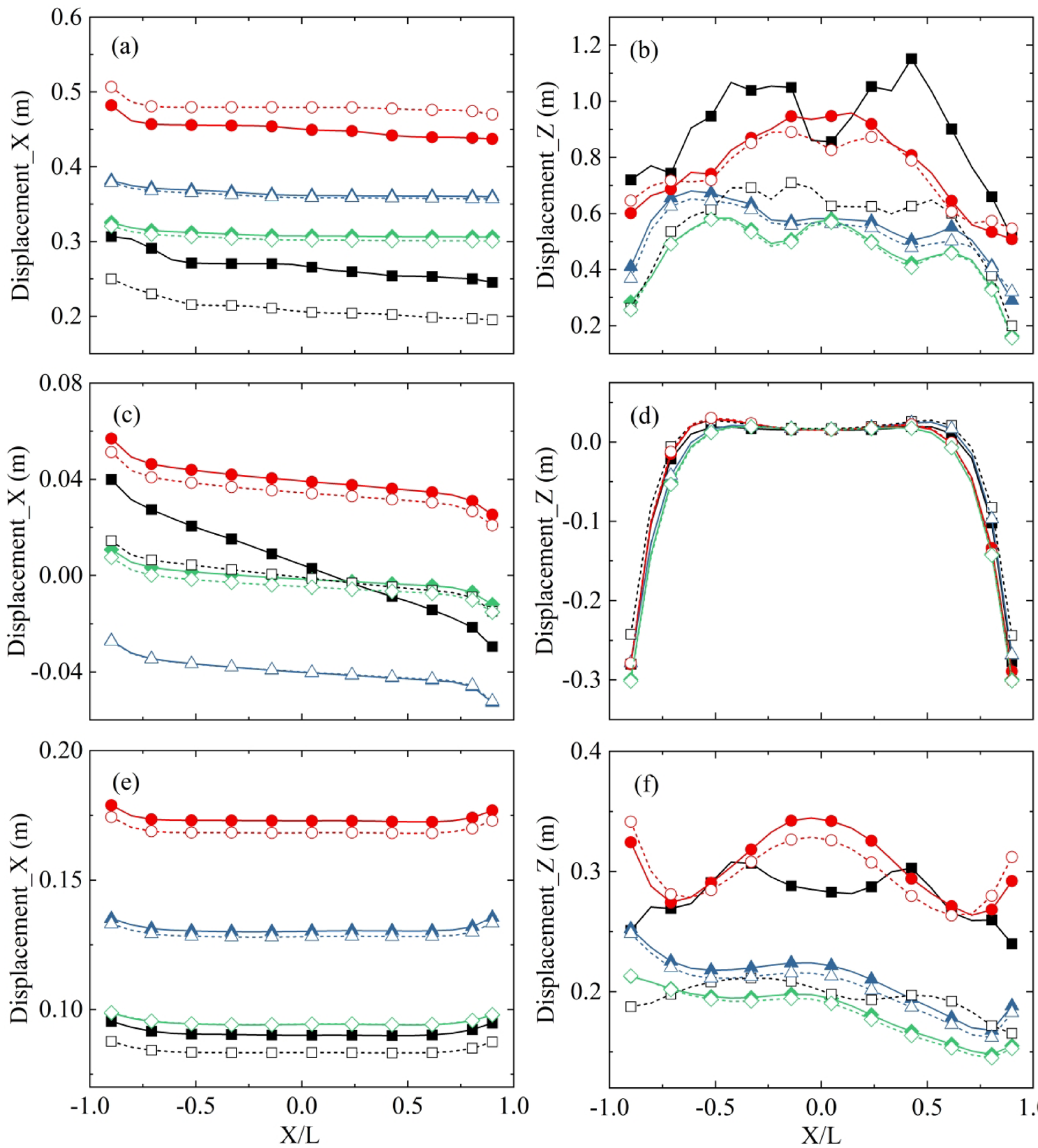

Fig. 7. Motion response of FSFs under load condition 1 (LC1) as listed in Table 1: maximum displacement in (**a**) X and (**b**) Z directions; average displacement in (**c**) X and (**d**) Z directions; and standard deviation in (**e**) X and (**f**) Z directions. Legend: dashed lines with hollow symbols = with internal WECs; solid lines with solid symbols = without internal WECs; black squares = no external WECs; blue triangles = front external WECs; red circles = rear external WECs; green diamonds = external WECs at both ends.

conditions. The joint loads of FSFs with WECs decrease to varying extents compared to those of FSF without WECs, with configurations incorporating internal WECs showing the most decrease. The maximum, mean, and STD of Fx for this configuration shows the decrease of 20%. Additionally, due to the wave absorption by internal and external WECs, the maximum value of Ry and the STD of the FSF with WECs are around 50% lower than those of the FSF without WECs.

Effects of mooring system

The impact of the mooring system is examined based on FSF with internal WECs and external WECs on both sides. This is because the vertical displacement of the FSF can be significantly mitigated due to the wave sheltering of external WECs and energy damping by internal WECs, while the horizontal displacement may increase due to the higher wave force on external WECs based on the last section. The environmental condition is chosen as LC3 to explore the dynamic response of WSW under extreme conditions. The mooring configuration for WSW is presented in Table 4. Additionally, the anchor depth and clump weight are studied. The anchor depth is adjustable, as part of the mooring cables of the WSW system can be connected to the OWT foundation, and

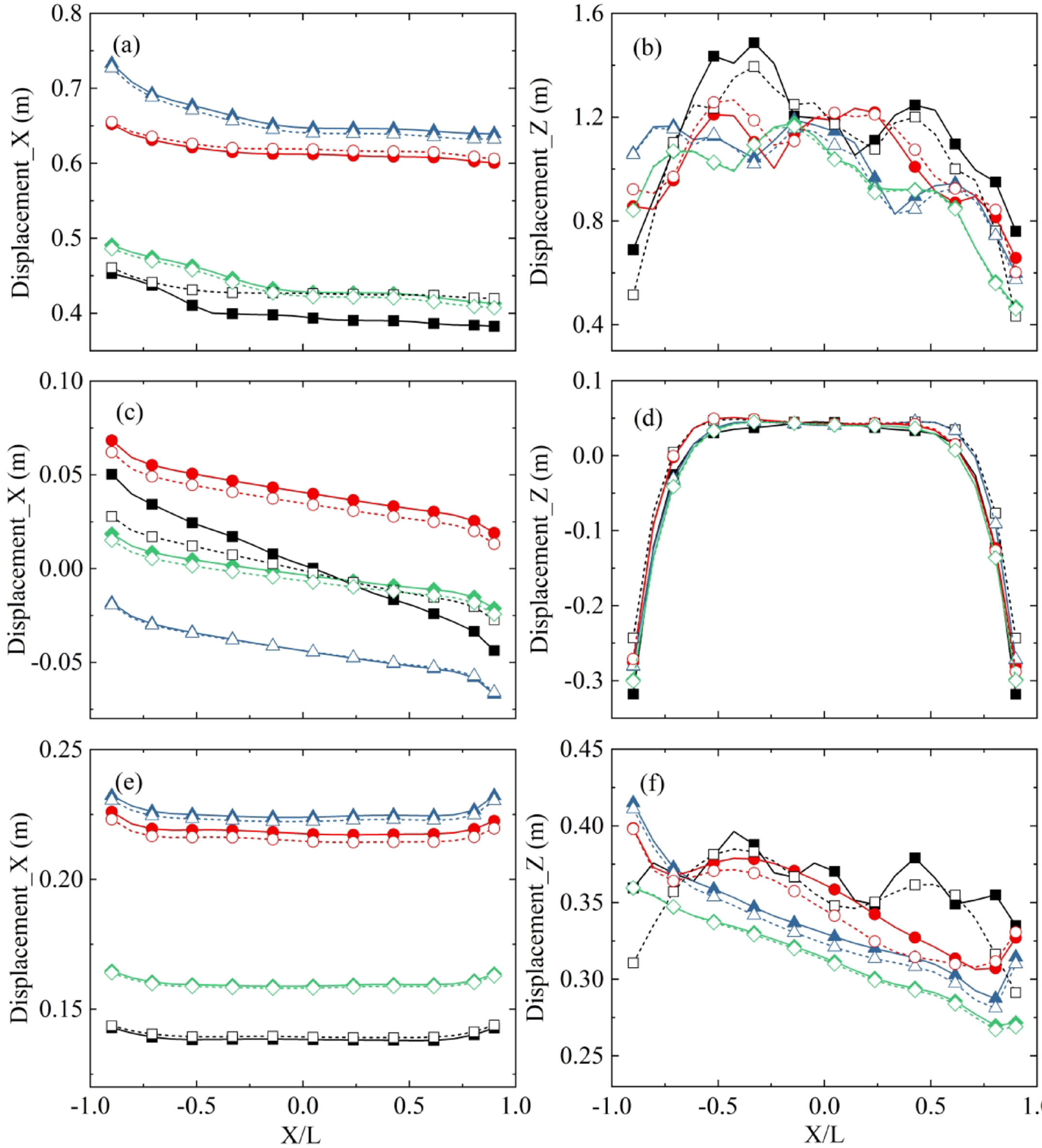

Fig. 8. Motion response of FSFs under LC2 as listed in Table 1: maximum displacement in (**a**) X and (**b**) Z directions; average displacement in (**c**) X and (**d**) Z directions; and standard deviation in (**e**) X and (**f**) Z directions. Legend: dashed lines with hollow symbols = with internal WECs; solid lines with solid symbols = without internal WECs; black squares = no external WECs; blue triangles = front external WECs; red circles = rear external WECs; green diamonds = external WECs at both ends.

the clump weight directly affects mooring line tension and platform stability. These factors are crucial for system stability and adaptability.

Mooring anchor depth

Figure 15 illustrates the impact of anchor depth on the horizontal and vertical motions of the FSF. The data clearly shows that the horizontal motion of the FSF is minimized, and stability is enhanced when the anchor depth is 0 m, indicating that the mooring cable is fully horizontal. At anchor depths of −4 m and – 20 m, the horizontal displacement is similar, with a maximum displacement of approximately 0.75 m and a STD of about 0.23 m. As the anchor depth increases, the system's control over horizontal motion declines, resulting in increased displacement and STD. The maximum vertical displacement of the FSF along the length at anchor depths of 0 m and – 20 m exhibits an opposing trend, due to insufficient vertical restraint from the horizontally placed mooring cables. As the anchor depth increases, vertical displacement at the ends of the FSF converges towards the center.

Figure 16 demonstrates the effect of anchor depths on the mooring cable tension. When the mooring cable is completely horizontal, the average tension exceeds 1000 kN, significantly higher than in other configurations,

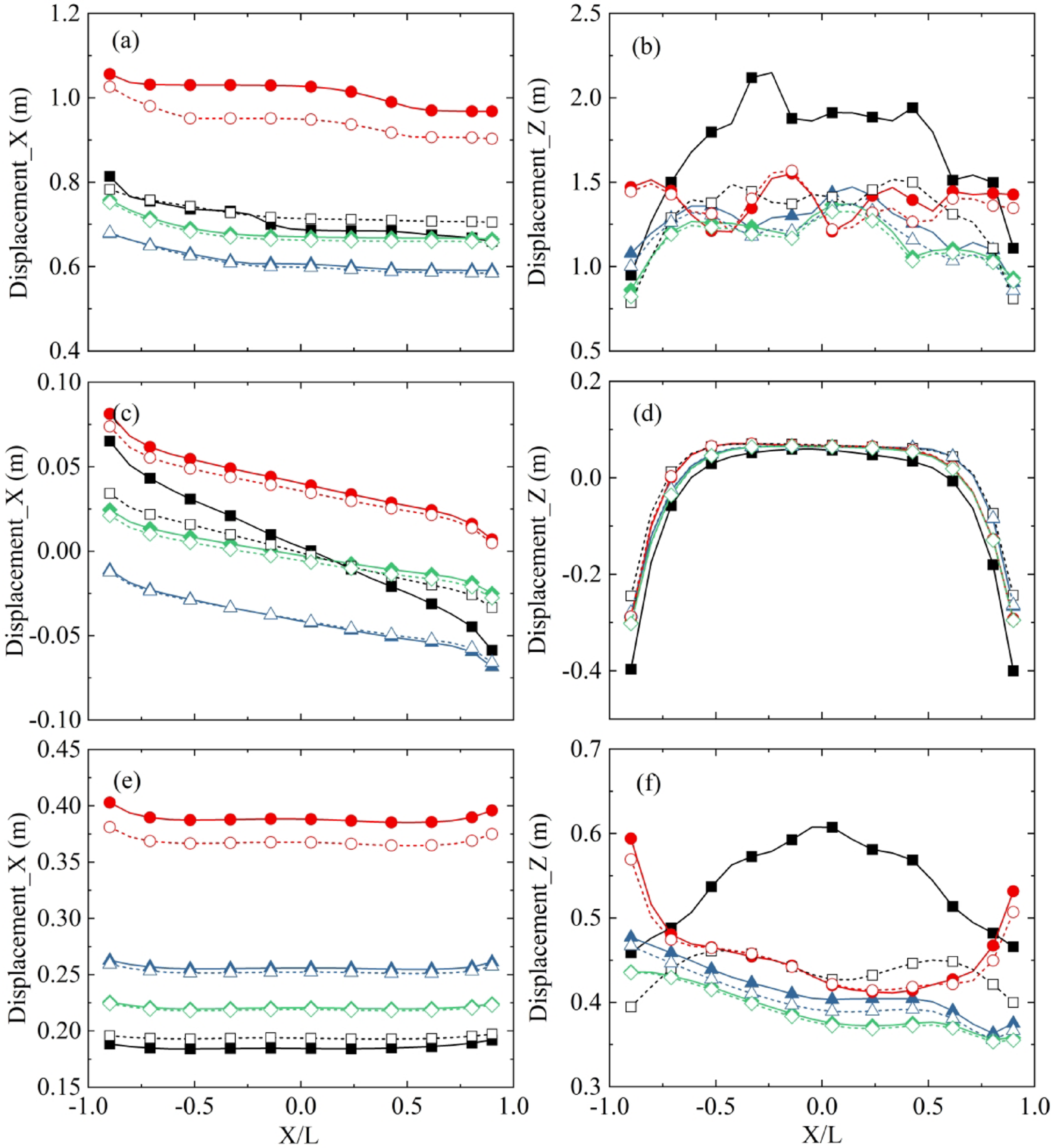

Fig. 9. Motion response of FSFs under LC3 as listed in Table 1: maximum displacement in (**a**) X and (**b**) Z directions; average displacement in (**c**) X and (**d**) Z directions; and standard deviation in (**e**) X and (**f**) Z directions. Legend: dashed lines with hollow symbols = with internal WECs; solid lines with solid symbols = without internal WECs; black squares = no external WECs; blue triangles = front external WECs; red circles = rear external WECs; green diamonds = external WECs at both ends.

presenting challenges for the long-term operation of the WSW system. This increase is due to the shorter mooring cable length at this height, resulting in higher tension for the same horizontal displacement. For anchor depths between 0 m and − 20 m, the average cable tension is lower than that of the original mooring solution. However, the maximum cable tensions for anchor depths of −8 m, −12 m, and − 16 m exceed 2000 kN, indicating a higher risk of cable breakage. In contrast, the mooring depth of −4 m exhibits better mooring tension than the original configuration, making it an acceptable choice.

Figure 17 depicts the effect of anchor depths on the joint loads of FSF's connectors. When the mooring cable is fully horizontal, the FSF is more susceptible to relative horizontal motions between modules, resulting in higher horizontal joint loads. Conversely, at an anchor depth of −4 m, both the mean and STD of the horizontal joint load are lower, suggesting reduced risk of horizontal crushing damage. As the anchor depth increases, the bending moment at both ends of the FSF decreases, with the motion response approximately inversely proportional to the internal force, where wave energy is dissipated as structural kinetic energy.

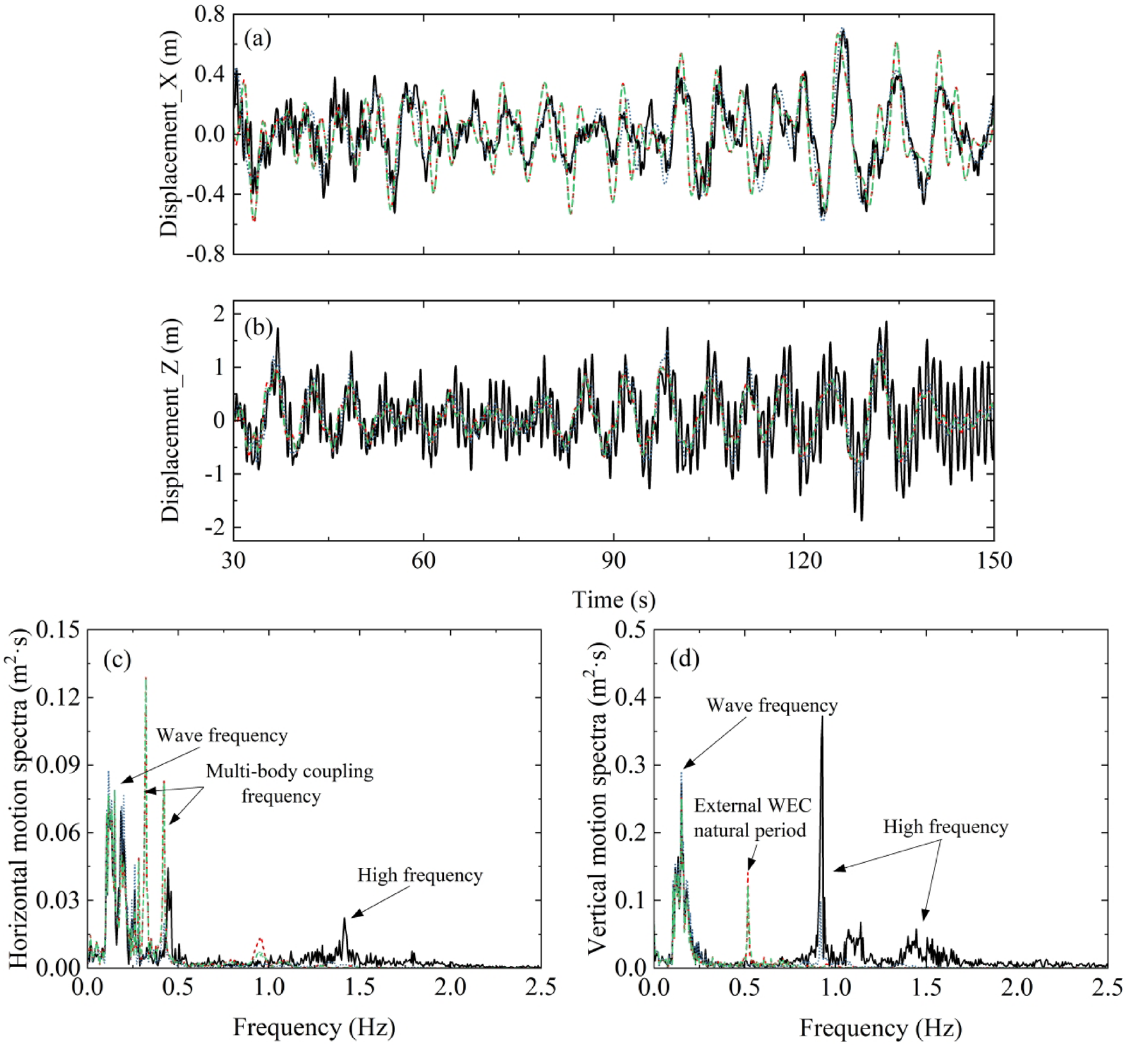

Fig. 10. Time history curves and motion spectra of WSWs under LC3: (**a**) horizontal and (**b**) vertical displacement time history curves; (**c**) horizontal and (**d**) vertical motion spectrum. Legend: black solid line = without WECs, red dashed line = external WECs at both ends, blue dotted line = internal WECs, green dash-dotted line = combined internal and external WECs.

Clump weight

Figure 18 demonstrates the effect of the clump weight on the horizontal and vertical motions of the FSF. The data reveal that while the installation of clumps minimally affects the average horizontal displacement of the FSF, it significantly influences motion amplitude and stability. Without clumps, the FSF exhibits high levels of maximum displacement and STD in the horizontal direction. Although clump installation helps control horizontal motion, excessive clump weights (2000 kg and 3000 kg) increase the angle between the mooring cable and the horizontal plane, reducing the horizontal tension component and weakening the mooring system's effectiveness. Clump installation markedly decreases the vertical motion amplitude of the FSF, enhancing stability. Variations in FSFs configured with different clump weights are indistinct, but as mooring tension increases, the floating bodies gradually submerge below the water level.

Figure 19 illustrates the effect of clump weight on mooring cable tension. As clump weight increases, the mean mooring cable tension rises, while the STD decreases. However, the maximum mooring cable tension diminishes as clump weight increases, reaching a minimum value of approximately 400 kN at a weight of 3000 kg, before gradually ascending again. This phenomenon results from the excessive angle formed between the upper mooring cable and the horizontal plane, weakening the cable's ability to restrain the FSF's horizontal motion, and leading to higher horizontal motion and mooring tension.

Figure 20 demonstrates the effect of clump weight on the joint loads in the FSF. Clump installation significantly reduces both the magnitude and fluctuation of horizontal joint loads, with the 3000 kg clump weight yielding the best horizontal joint force performance. However, excessive clump weight tightens the mooring cable, altering its angle and reducing the horizontal tension component, weakening its restraint on horizontal motion. The average joint bending moments at both ends of the FSF increase with clump weight, while clump installation has minimal effect on vertical displacement.

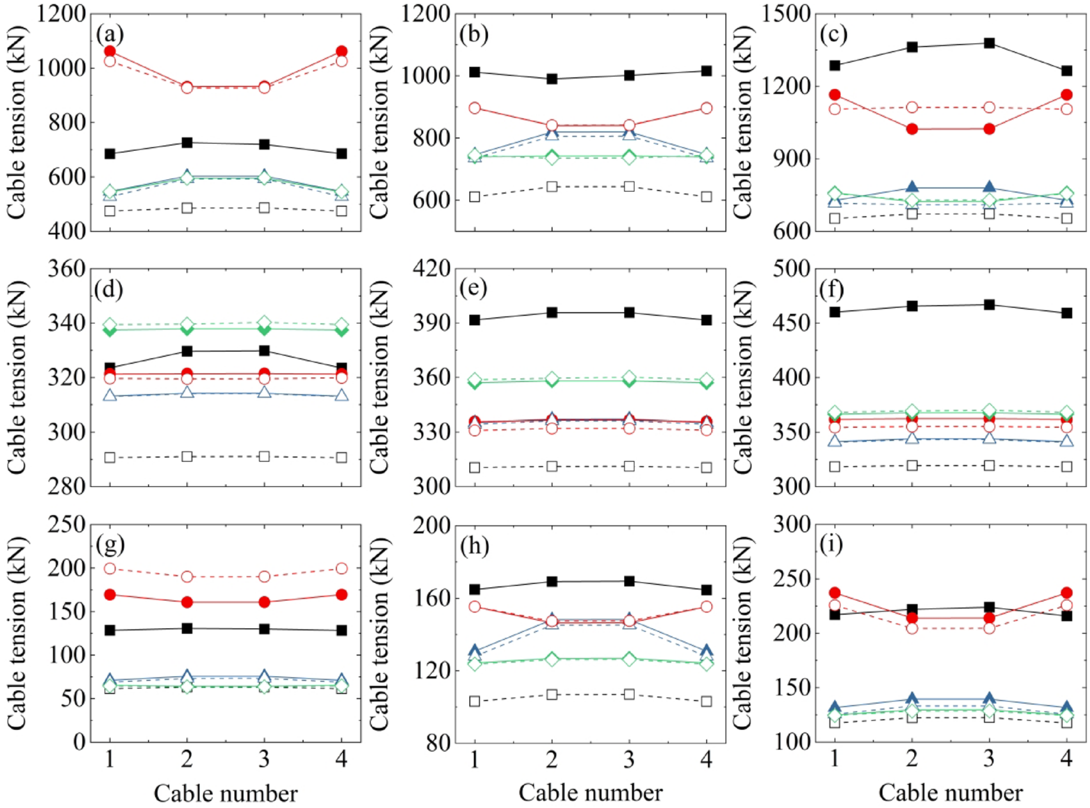

Fig. 11. Cable tension for FSFs under three LCs: Maximum cable tension with (**a**) LC1, (**b**) LC2, and (**c**) LC3; Average cable tension with (**d**) LC1, (**e**) LC2, and (**f**) LC3; (**g**) Standard deviation with (**g**) LC1, (**h**) LC2, and (**i**) LC3. Legend: dashed lines with hollow symbols = with internal WECs, solid lines with solid symbols = without internal WECs, black squares = no external WECs, blue triangles = front external WECs, red circles = rear external WECs, green diamonds = external WECs at both ends.

Power output

The potential power output by the WSW is examined in this section. The wind speeds for three LCs are assumed to exceed the rated wind speed of 11.4 m/s in the present study. The wind turbine hub is positioned high enough above the sea surface, making it insignificantly affected by the WECs and FSF. Bi et al.[58] showed that the effect of high wind and waves on the solar power generation of PV panels is negligible, with the relative change in total power output remaining within 0.2%–0.5% under different offshore wind-generated wave conditions. Hence, we applied their conclusion in the present study by assuming a constant power output of FSF panels. A prototype floating platform unit adopted has dimensions of 16.5 m in width and 63 m in length, comprising a total array of 13 modules in width and 50 modules in length. Therefore, a single FSF unit can have a total capacity of 300 W×13 × 50 = 195 kW.

The power output is evaluated based on the practical offshore installation as shown in Fig. 21. The study assumes an offshore wind farm comprising four 5 MW OWTs. The spacing between OWTs along the wind direction is set at eight times the rotor diameter (~1040 m), while the lateral spacing between neighboring OWTs is four times the rotor diameter (~500 m). To optimize the use of vacant sea space, eight FSFs are deployed between the OWTs. Each FSF measures 240 m × 240 m, with a 20 m gap to accommodate operation and maintenance (O&M) vessel passage, covering 88.6% of the vacant sea area in total. Assuming constant power generation efficiency for each FSF, the total PV power output is estimated at 86,442 kW. The installation also includes internal and external WECs positioned around and within the FSFs.

The power output of WECs is calculated while accounting for wave attenuation due to the wave-sheltering effects of upstream FSF units. The relative motions and velocities of each WEC in the WSW system from the simulations are used to determine the power output of the most upstream FSF unit. This output serves as the basis for calculating the power generation for different LCs using the equations given in Eqs. (2) and (3). The results are then employed to extrapolate the power efficiency of downstream WECs by considering the linear decay rate of WEC power output across the full-scale WSW system, as shown in Fig. 21. The decay rate is calculated as follows:

$$\eta_d = \frac{P_{upstream} - P_{downstream}}{P_{upstream} \cdot d} \tag{6}$$

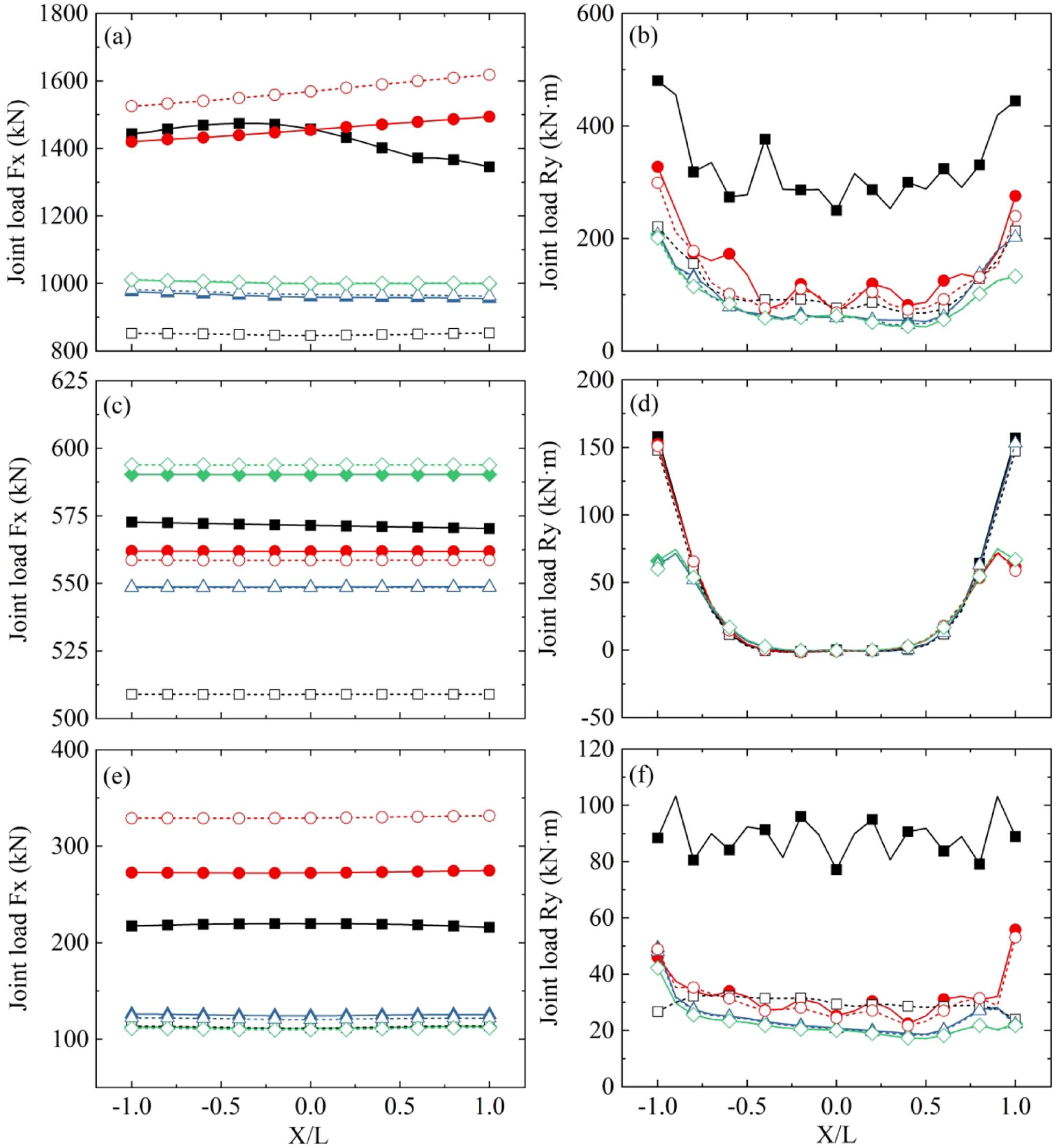

Fig. 12. Joint loads for FSFs with LC1: Maximum joint load in (**a**) X and (**b**) Z directions; Average joint load in (**c**) X and (**d**) Z directions; Standard deviation in (**e**) X and (**f**) Z directions. Legend: dashed lines with hollow symbols = with internal WECs, solid lines with solid symbols = without internal WECs, black squares = no external WECs, blue triangles = front external WECs, red circles = rear external WECs, green diamonds = external WECs at both ends.

where η_d denotes the linear decay rate of power output per unit length. $P_{upstream}$ and $P_{downstream}$ represent the power output of upstream and downstream WECs, respectively. d is the distance between upstream and downstream WECs. For the three LCs investigated, the linear decay rates per unit length of the external WEC were 0.79%, 0.56%, and 0.63%, respectively. The internal WECs exhibited different decay characteristics due to the interaction with the surrounding structure. Therefore, the linear decay rates per unit length of the internal WECs were calculated based on the average values at their respective locations, with values of 5.85%, 4.15%, and 5.61%, respectively. Using these linear attenuation rates, the power output of downstream WEC at any location in the full-scale WSW system can be extrapolated, provided that the power output of upstream WEC is known, and can be expressed as

$$P_{\text{downstream},\ i} = P_{\text{upstream}} - \eta_d \cdot P_{\text{upstream}} \cdot d_i \tag{7}$$

where, $P_{downstream,\ i}$ represents the power output of the ith downstream WEC. d_i is represents the distance between the ith downstream WEC and the upstream WEC. $\eta_d$denotes the linear decay rate per unit length, as

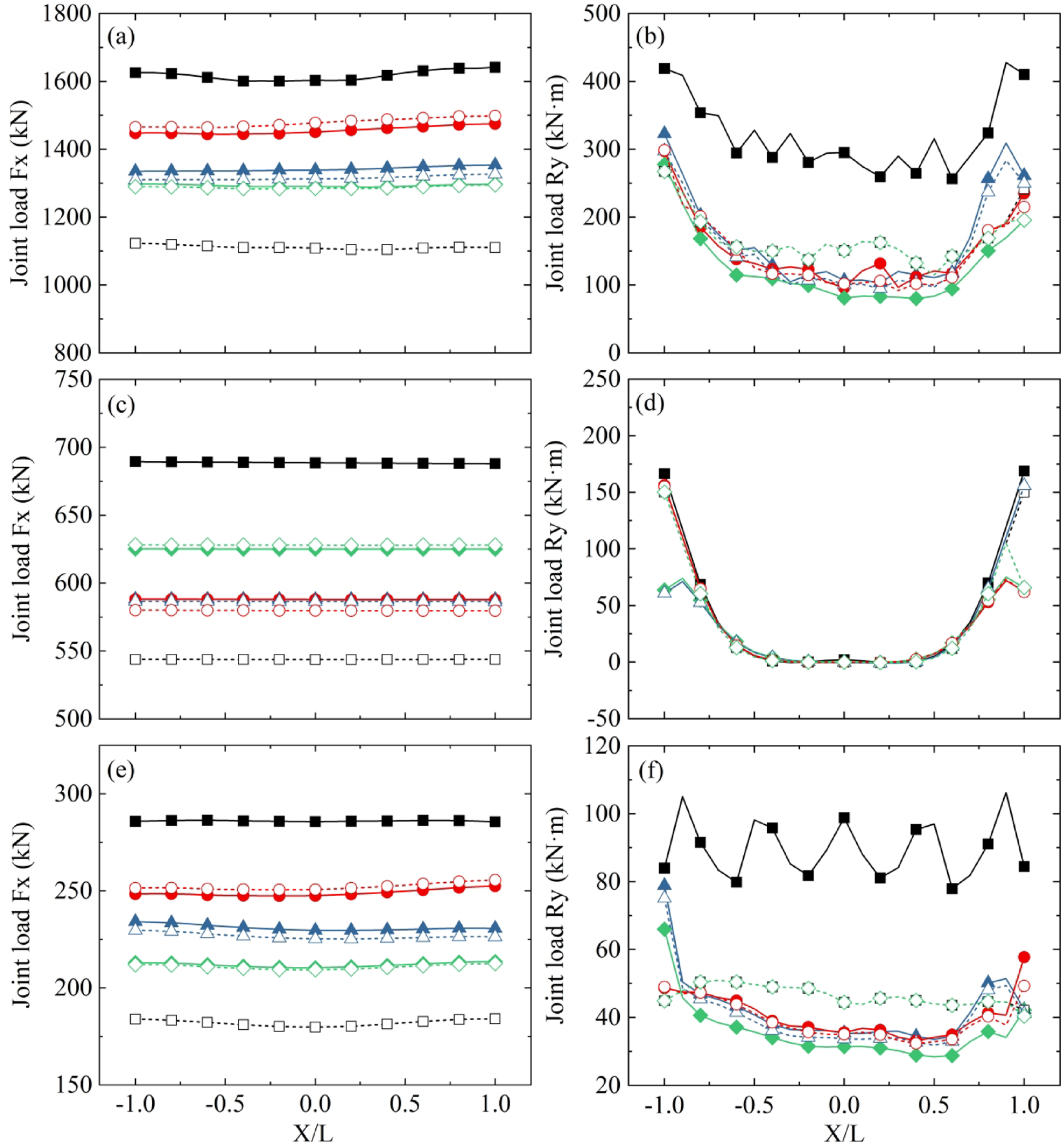

Fig. 13. Joint loads for FSFs with LC2: Maximum joint load in (**a**) X and (**b**) Z directions; Average joint load in (**c**) X and (**d**) Z directions; Standard deviation in (**e**) X and (**f**) Z directions. Legend: dashed lines with hollow symbols = with internal WECs, solid lines with solid symbols = without internal WECs, black squares = no external WECs, blue triangles = front external WECs, red circles = rear external WECs, green diamonds = external WECs at both ends.

defined in Eq. (6). Furthermore, by aggregating the power output of all individual WECs, the total wave energy generation in the WSW P_{total} can be estimated and can be expressed as:

$$P_{\text{total}} = P_{\text{upstream}} + \sum_{i=1}^{n} P_{\text{downstream},\ i} \tag{8}$$

where, n is the total number of downstream WECs. As a result, the estimated power generation of the WECs is 13,560 kW, 24,285 kW, and 31,071 kW for three LCs, respectively. It should be noted that the WEC power generation estimates exclude contributions from lateral WECs, and the power output from downstream WECs is expected to be minimal based on linear decay rates. However, wave diffraction and radiation effects enable downstream WECs to contribute significantly to overall power output, which is also not accounted for in the estimates. As a result, the estimated WEC generation remains highly conservative.

Figure 22 compares the power generation of WECs in a full-scale WSW farm under three LCs with the power output of OWTS and FSFs as reference. Table 5 presents the power contributions of each component and the total output for the three LCs. The results show that external WECs consistently demonstrate higher generation,

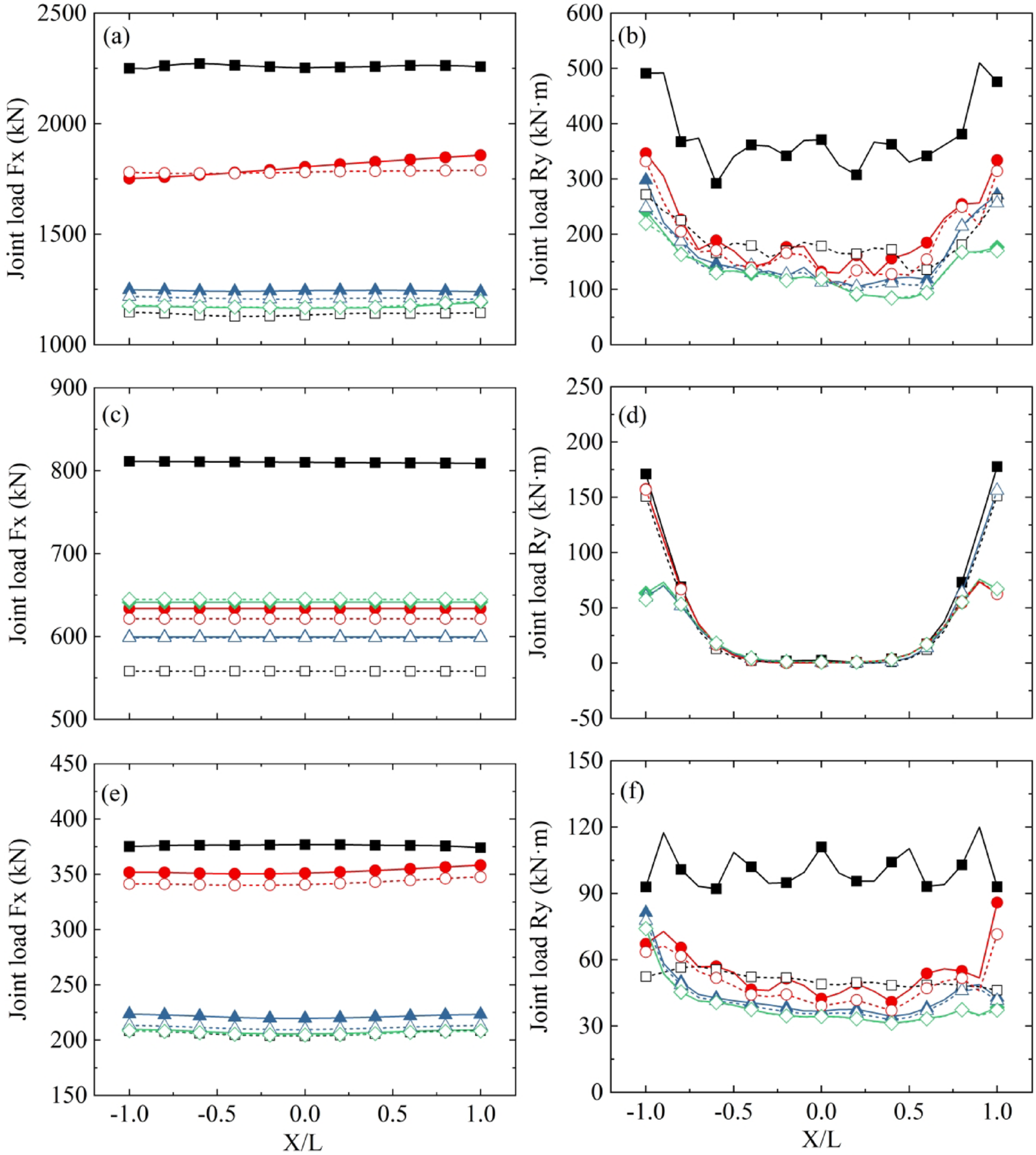

Fig. 14. Joint loads for FSFs with LC3: Maximum joint load in (**a**) X and (**b**) Z directions; Average joint load in (**c**) X and (**d**) Z directions; Standard deviation in (**e**) X and (**f**) Z directions. Legend: dashed lines with hollow symbols = with internal WECs, solid lines with solid symbols = without internal WECs, black squares = no external WECs, blue triangles = front external WECs, red circles = rear external WECs, green diamonds = external WECs at both ends.

primarily due to their exposure to stronger relative motion at the farm's periphery. As sea states intensify, the external WEC output continues to rise, whereas the internal WEC output stabilizes. This highlights the protective role of external WECs, which help limit wave energy transmission to the FSF, potentially extending its operational lifespan. Despite the contribution of WECs, the FSF remains the dominant power source, significantly surpassing the combined WEC outputs. However, wave energy constitutes a substantial portion of the total power mix, ranging from 11.3% to 22.6% across the three LCs. This share is particularly notable given that the estimates exclude contributions from lateral WECs as well as wave diffraction and radiation effects. These findings underscore the importance of integrating WECs into the farm's design, as they not only enhance wave energy capture but also reduce structural loads on the FSF, improving system safety and long-term performance.

The power output curves of the WECs were obtained across a broader wind speed range by fitting and extrapolating the simulation data. These curves were then compared with the total power generation of the wind turbines, solar farm, and the integrated WSW system, as shown in Fig. 23. The figure illustrates the WEC power generation trends under different LCs and clarifies the relative contribution of each energy device. In addition,

Mooring configuration	Mooring stiffness (kN/m)	Mooring anchor depth (m)	Cable length (m)	Clump position from connection point (m)	Clump weight (kg)	Objectives
1	2250	0	34.06	7.023	0	To determine the effect of mooring anchor depth on WSW
2		−4	35.114			
3		−8	36.168			
4		−12	37.222			
5		−16	38.276			
6		−20	39.33			
7		−4	35.114		1000	To determine the effect of clump weight on WSW
8					2000	
9					3000	
10					4000	
11					5000	

Table 4. Mooring configurations.

the probability distribution of the LCs is included, enabling an assessment of the generation capacity and output share of each energy type under varying sea states.

Conclusions

This study examines the structural stability and power performance of a novel WSW co-generation system, which integrates OWTs, FSFs, and WECs. The system is designed to maximize renewable production energy per unit area of the permitted site area while enhancing overall structural stability of the system. A multi-body hydrodynamic interaction numerical model is developed to comprehensively examine the dynamic characteristics of various WSW configurations under a range of operating conditions, from mild to extreme. The key findings and design recommendations are summarized as follows:

1. WECs should be symmetrically installed in a mesh configuration both inside and around the FSF to minimize vertical and horizontal displacements, reduce joint loads, and stabilize mooring tension. Their installations can enable wave energy absorption, decrease internal structural loads, and protect the FSF from severe wave impacts.
2. Reducing anchor depth by mooring the structure to the foundation of OWTs can effectively control structural motion and promote a more uniform distribution of bending moments. However, a fully horizontal mooring cable significantly increases mooring tension and should be avoided. A moderate increase in clump weight, recommended at 0.6–0.9 times the weight of a WEC, can further reduce mooring tension and improve horizontal motion control.
3. The configuration of WECs should be adapted to the specific environmental conditions and structural dimensions of the FSF. When the incident wavelength is comparable to the FSF's scale, the wave-sheltering effect of WECs will become less effective. Optimizing the placement and type of WECs based on prevailing wave conditions and sea states is essential for achieving effective load reduction and ensuring structural stability.
4. The integration of WECs contributes a significant component of 11.3% to 22.6% of the total WSW output power generation with different LCs.

The WSW concept proposed in this study demonstrates strong potential for optimizing motion performance and maximizing renewable energy production in hybrid co-generation systems. Further research should focus on the optimisation of combining the different technologies and validating the system through experimentation and pilot field studies.

Several limitations and assumptions need to be acknowledged. First, the present analysis is confined to normal operating conditions and does not account for extreme events such as hurricanes, during which PV modules may need to be disconnected or WECs temporarily lifted for protection. Wind loads on PV panels were also neglected, although they could strongly affect system stability in windy offshore sites. In addition, practical implementation aspects, including maintenance, component durability, and installation logistics, remain to be addressed. For example, while mooring FSFs to existing monopiles is logistically attractive, the additional loads on foundations must be verified. Similarly, integrating PV and WEC cabling with wind turbine infrastructure could reduce the cost of energy but requires reliable control systems to manage three energy devices in parallel. Finally, future work should also consider the techno-economic optimization to determine cost-efficient configurations with the optimal number of devices.

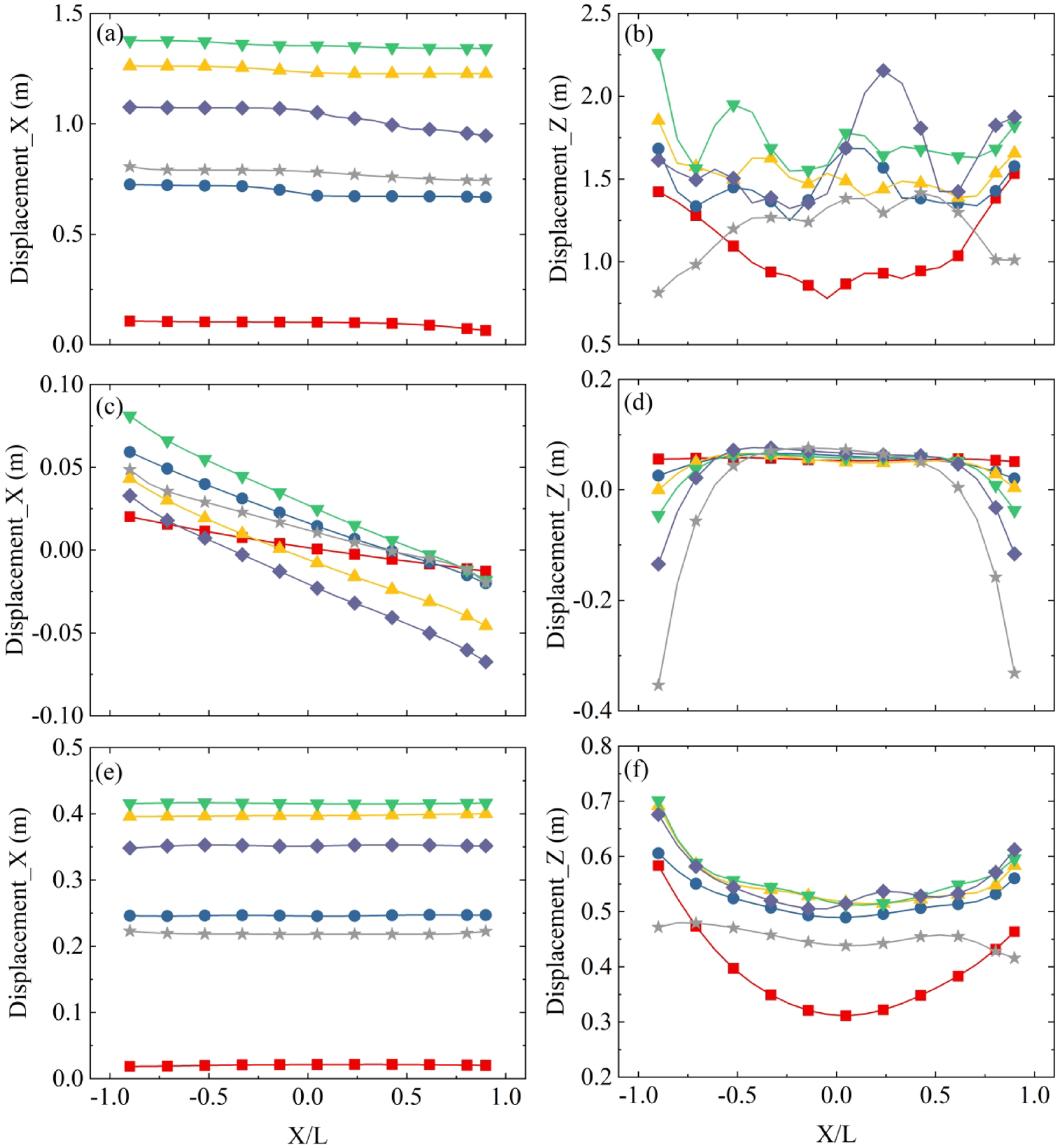

Fig. 15. Displacement of WSWs with different mooring anchor depths: Maximum displacement in (**a**) X and (**b**) Z directions, Average displacement in (**c**) X and (**d**) Z directions, Standard deviation in (**e**) X and (**f**) Z directions. Legend: red line with squares = 0 m, blue line with circles = −4 m, yellow line with triangles = −8 m, green line with inverted triangles = −12 m, purple line with diamonds = −16 m, grey line with stars = −20 m.

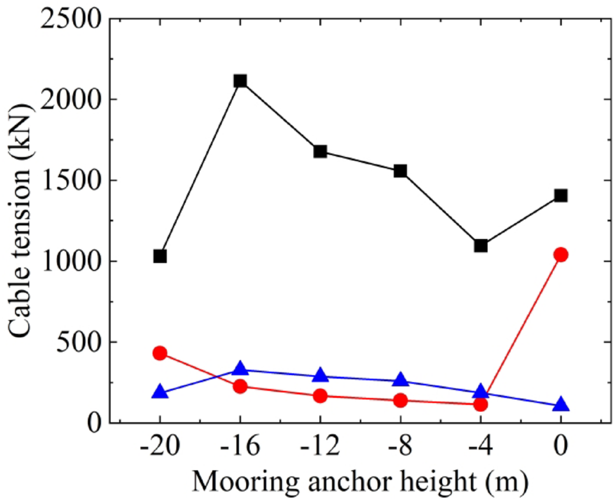

Fig. 16. Cable tension of WSW with different mooring anchor depths. Legend: black line with squares = maximum value, red line with circles = average, blue line with triangles = standard deviation.

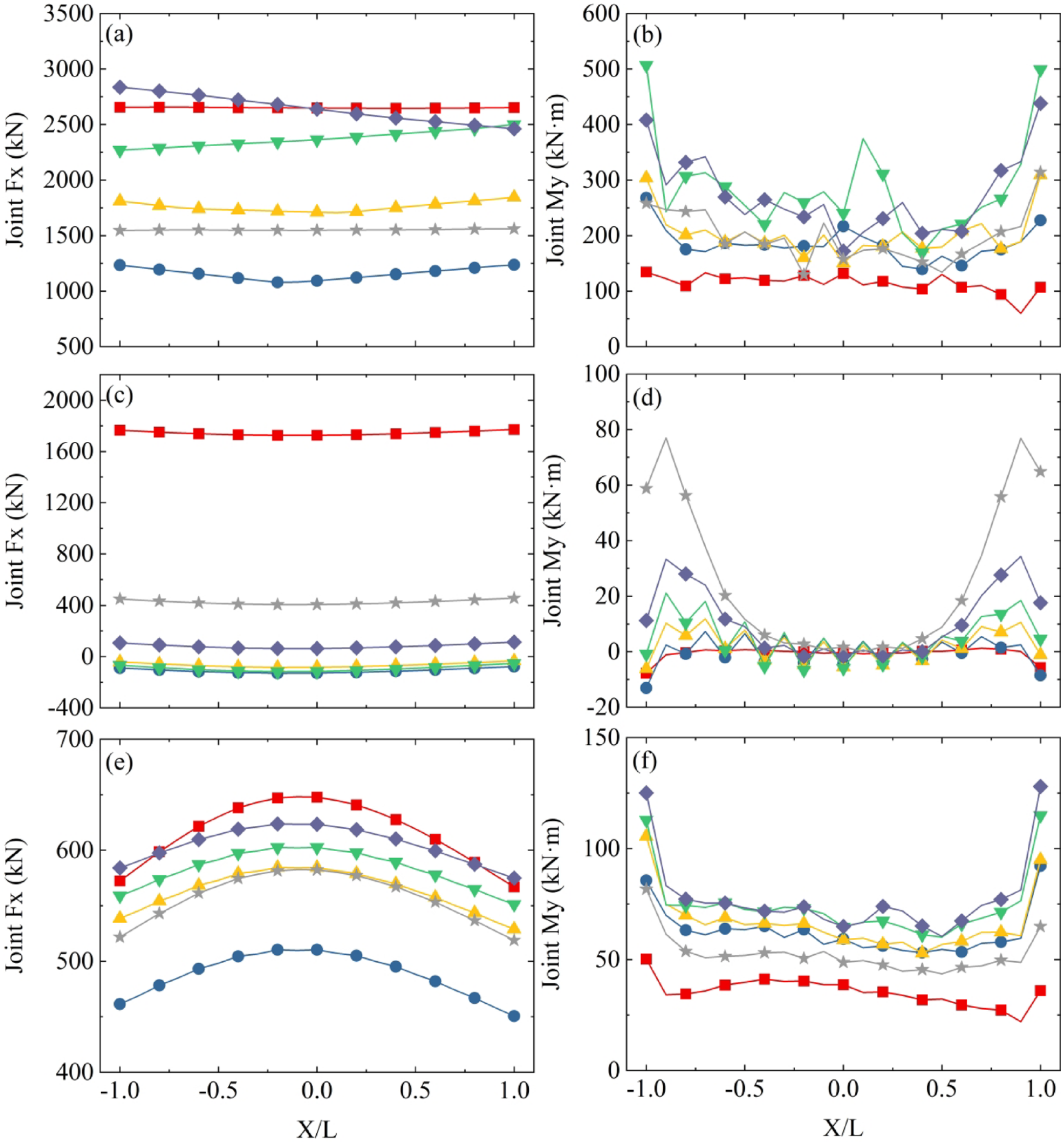

Fig. 17. Joint load of WSWs with different mooring anchor depths: Maximum joint load in (**a**) X and (**b**) Z directions, Average joint load in (**c**) X and (**d**) Z directions, Standard deviation of joint loads in (**c**) X and (**d**) Z directions. Legend: red line with squares = 0 m, blue line with circles = −4 m, yellow line with triangles = −8 m, green line with inverted triangles = −12 m, purple line with diamonds = −16 m, grey line with stars = −20 m.

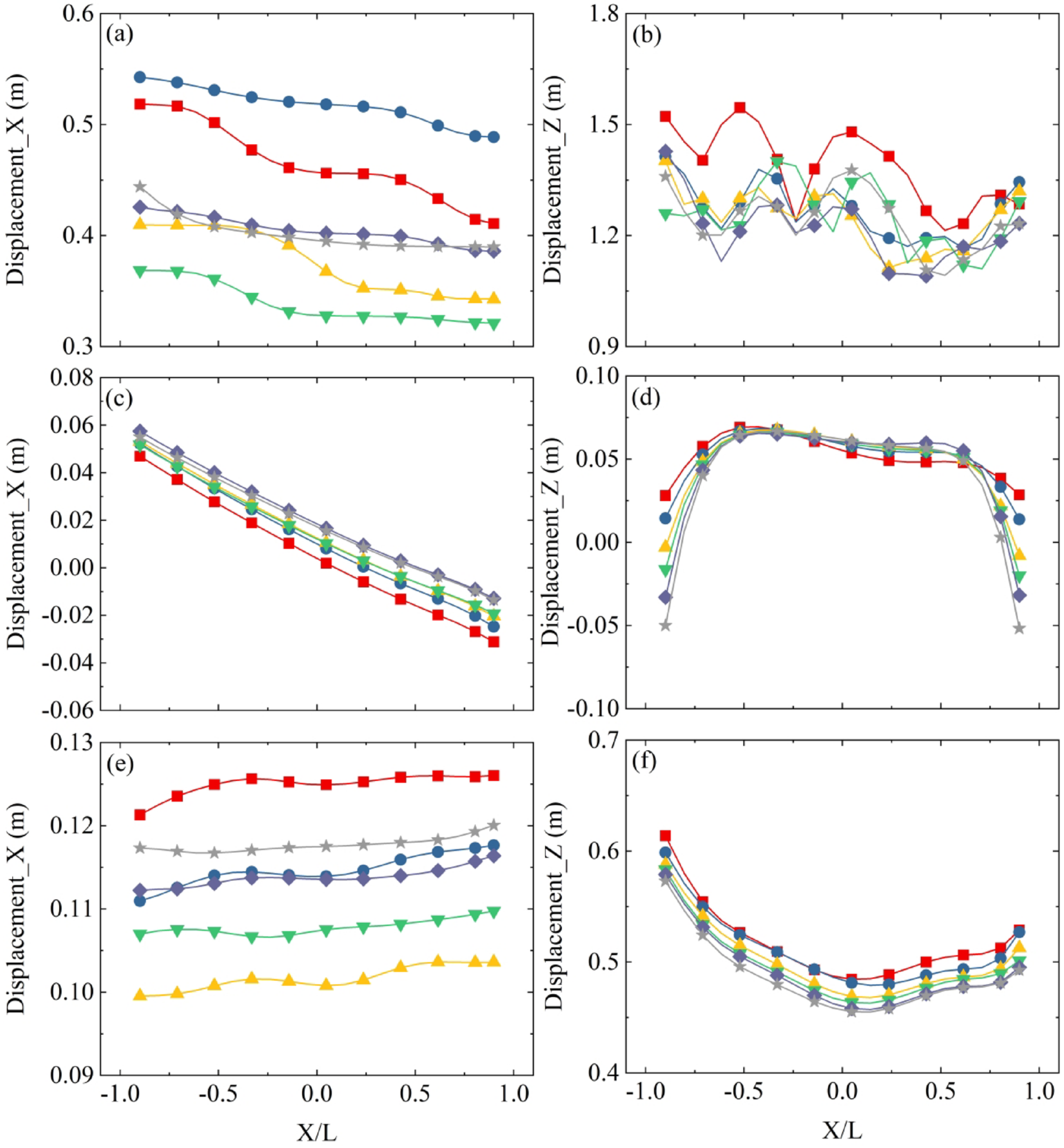

Fig. 18. Displacement of WSWs with different clump weights: Maximum displacement in (**a**) X and (**b**) Z directions, Average displacement in (**c**) X and (**d**) Z directions, Standard deviation in (**e**) X and (**f**) Z directions. Legend: red line with squares = No clump, blue line with circles = 1000 kg, yellow line with triangles = 2000 kg, green line with inverted triangles = 3000 kg, purple line with diamonds = 4000 kg, grey line with stars = 5000 kg.

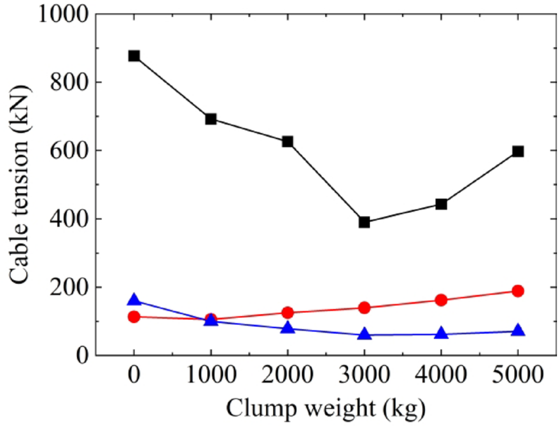

Fig. 19. Cable tension of WSW under different clump weights. Legend: black line with squares = maximum value, red line with circles = average, blue line with triangles = standard deviation.

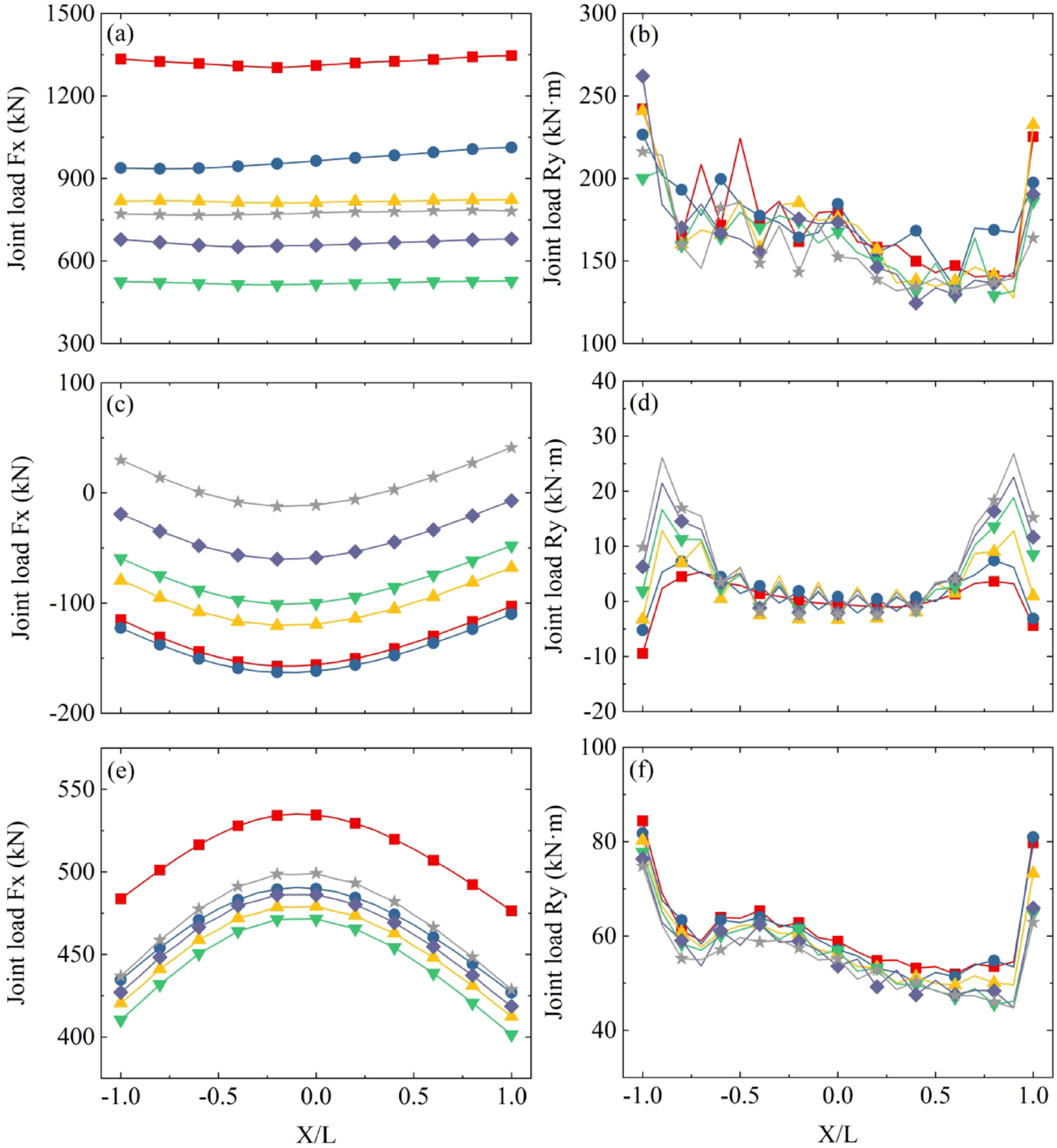

Fig. 20. Joint load of WSWs under different clump weights: Maximum joint load in (**a**) X and (**b**) Z directions, Average joint load in (**c**) X and (**d**) Z directions, Standard deviation of joint load in (**c**) X and (**d**) Z directions. Legend: red line with squares = No clump, blue line with circles = 1000 kg, yellow line with triangles = 2000 kg, green line with inverted triangles = 3000 kg, purple line with diamonds = 4000 kg, grey line with stars = 5000 kg.

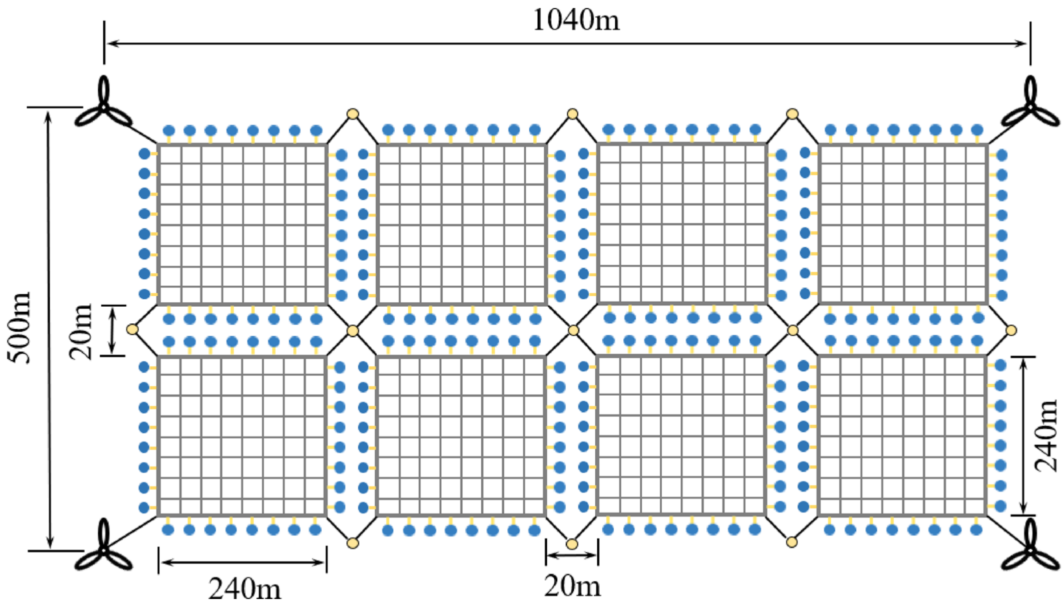

Fig. 21. Schematic layout of a real-scale WSW farm.

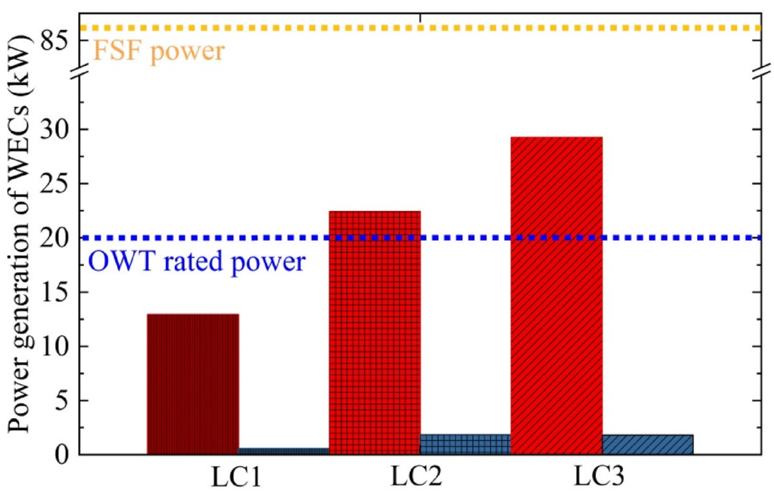

Fig. 22. Power generation for the real-scale WSW farm with three LCs. Legend: red bars = power generated by external WECs, blue bars = power generated by internal WECs.

LC	OWTs power (MW)	FSFs power (MW)	External WECs power (MW)	Internal WECs power (MW)	Total power (MW)	WEC share (%)
LC1	20	86.4	13.0	0.59	120.0	11.3
LC2	20	86.4	22.4	1.85	130.7	18.6
LC3	20	86.4	29.3	1.81	137.5	22.6

Table 5. Power contributions of WTs, FSFs, and WECs under different LCs.

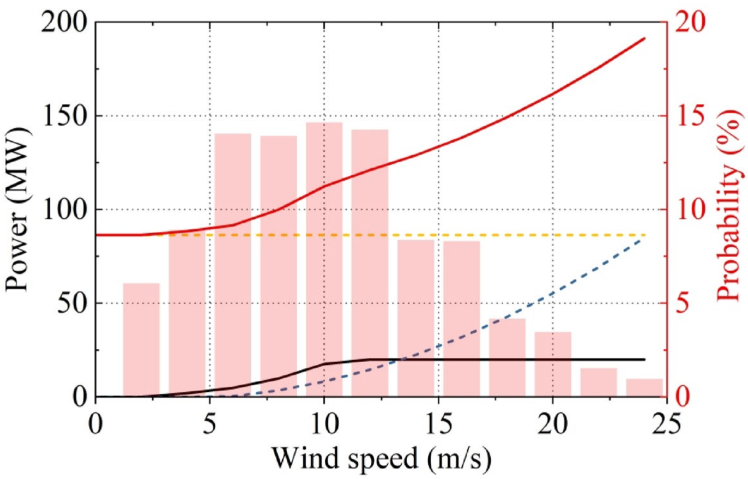

Fig. 23. Power curve of the WSW system. Legend: black solid line = wind power, yellow dash line = solar power, blue dash line = wave power, red solid line = total power, red bars = occurrence probability of load conditions.

Data availability

The datasets used and/or analysed during the current study available from the corresponding author on reasonable request.

Received: 17 August 2025; Accepted: 27 November 2025
Published online: 15 December 2025

References

1. Musial, W. et al. *Offshore wind market report: 2023 edition (No. NREL/TP-5000-87232)*. (National Renewable Energy Lab. (NREL), 2023).
2. Erkan, O., Özkan, M., Karakoç, T. H., Garrett, S. J. & Thomas, P. J. Investigation of aerodynamic performance characteristics of a wind-turbine-blade profile using the finite-volume method. *Renew. Energ.* **161**, 1359–1367 (2020).
3. Boye, T. E. & Xie, Z. T. Aerodynamics of a pitching wind turbine blade at high reduced frequencies. *J. Wind Eng. Ind. Aerod.* **223**, 104935 (2022).
4. Li, Z. et al. Aerodynamic and aeroelastic characteristics of flexible wind turbine blades under periodic unsteady inflows. *J. Wind Eng. Ind. Aerod.* **197**, 104057 (2020).
5. Ji, B. et al. CFD simulations of aerodynamic characteristics for the three-blade NREL phase VI wind turbine model. *Energy* **249**, 123670 (2022).
6. Cao, G., Chen, Z., Wang, C. & Ding, X. Dynamic responses of offshore wind turbine considering soil nonlinearity and wind-wave load combinations. *Ocean. Eng.* **217**, 108155 (2020).
7. Xi, R. et al. Framework for dynamic response analysis of monopile supported offshore wind turbine excited by combined wind-wave-earthquake loading. *Ocean. Eng.* **247**, 110743 (2022).
8. Mo, R., Cao, R., Liu, M. & Li, M. Effect of ground motion directionality on seismic dynamic responses of monopile offshore wind turbines. *Renew. Energ.* **175**, 179–199 (2021).
9. Wang, P., Xu, Y., Zhang, X., Xi, R. & Du, X. A substructure method for seismic responses of offshore wind turbine considering nonlinear pile-soil dynamic interaction. *Soil. Dyn. Earthq. Eng.* **144**, 106684 (2021).
10. Shittu, A. A. et al. Structural reliability assessment of offshore wind turbine support structures subjected to pitting corrosion-fatigue: A damage tolerance modelling approach. *Wind Energy*. **23** (11), 2004–2026 (2020).
11. Bhattacharya, S. et al. Physical modelling of offshore wind turbine foundations for TRL (technology readiness level) studies. *J. Mar. Sci. Eng.* **9** (6), 589 (2021).
12. Katsikogiannis, G., Sørum, S. H., Bachynski, E. E. & Amdahl, J. Environmental lumping for efficient fatigue assessment of large-diameter monopile wind turbines. *Mar. Struct.* **77**, 102939 (2021).
13. Yeter, B. & Garbatov, Y. Structural integrity assessment of fixed support structures for offshore wind turbines: A review. *Ocean. Eng.* **244**, 110271 (2022).
14. Tang, Z. H. et al. Countermeasures for local scour at offshore wind turbine monopile foundations: A review. *Water Sci. Eng.* **15** (1), 15–28 (2022).
15. Li, J., Guo, Y., Lian, J. & Wang, H. Mechanisms, assessments, countermeasures, and prospects for offshore wind turbine foundation scour research. *Ocean. Eng.* **281**, 114893 (2023).
16. Mayall, R. O. et al. Flume tank testing of offshore wind turbine dynamics with foundation scour and scour protection. *J. Waterw Port Coast*. **146** (5), 04020033 (2020).
17. Ma, H. & Chen, C. Scour protection assessment of monopile foundation design for offshore wind turbines. *Ocean. Eng.* **231**, 109083 (2021).
18. Tayel, S. A., Abu El-Maaty, A. E., Mostafa, E. M. & Elsaadawi, Y. F. Enhance the performance of photovoltaic solar panels by a self-cleaning and hydrophobic Nanocoating. *Sci. Rep-UK*. **12** (1), 21236 (2022).
19. Yun, M. J., Sim, Y. H., Cha, S. I., Seo, S. H. & Lee, D. Y. Three-dimensional textile platform for electrochemical devices and its application to dye-sensitized solar cells. *Sci. Rep-UK*. **9** (1), 2322 (2019).
20. IEA. *Snapshot 2023—IEA-PVPS*. https://iea-pvps.org/snapshot-reports/snapshot-2023/ (2024).
21. Micheli, L. The temperature of floating photovoltaics: case studies, models and recent findings. *Sol Energy*. **242**, 234–245 (2022).
22. Lee, N. et al. Hybrid floating solar photovoltaics-hydropower systems: benefits and global assessment of technical potential. *Renew. Energ.* **162**, 1415–1427 (2020).

23. Jin, Y. et al. Energy production and water savings from floating solar photovoltaics on global reservoirs. *Nat. Sustain.* **6** (7), 865–874 (2023).
24. Sanchez, R. G., Kougias, I., Moner-Girona, M., Fahl, F. & Jäger-Waldau, A. Assessment of floating solar photovoltaics potential in existing hydropower reservoirs in Africa. *Renew. Energ.* **169**, 687–699 (2021).
25. López, M., Soto, F. & Hernández, Z. A. Assessment of the potential of floating solar photovoltaic panels in bodies of water in Mainland Spain. *J. Clean. Prod.* **340**, 130752 (2022).
26. Yang, R. Y. & Yu, S. H. A study on a floating solar energy system applied in an intertidal zone. *Energies* **14** (22), 7789 (2021).
27. Ma, G. et al. Hydrodynamic analysis of floating photovoltaic system constrained with rigid connectors. *Sci. Rep-UK*. **14** (1), 29920 (2024).
28. Magkouris, A., Rusu, E., Rusu, L. & Belibassakis, K. Floating solar systems with application to nearshore sites in the Greek sea region. *J. Mar. Sci. Eng.* **11** (4), 722 (2023).
29. Sree, D. K. et al. Fluid-structural analysis of modular floating solar farms under wave motion. *Sol Energy*. **233**, 161–181 (2022).
30. Zeng, F. et al. An adaptive Barrier-Mooring system for coastal floating solar farms. *Appl. Energ.* **348**, 121618 (2023).
31. Nguyen, H. P., Wang, C. M., Tay, Z. Y. & Luong, V. H. Wave energy converter and large floating platform integration: A review. *Ocean. Eng.* **213**, 107768 (2020).
32. Castro-Santos, L., Martins, E. & Soares, C. G. Economic comparison of technological alternatives to Harness offshore wind and wave energies. *Energy* **140**, 1121–1130 (2017).
33. Zhang, H., Zhang, N. & Cao, X. Conceptualization and dynamic response of an integrated system with a semi-submersible floating wind turbine and two types of wave energy converters. *Ocean. Eng.* **269**, 113517 (2023).
34. Hu, J. et al. Optimal design and performance analysis of a hybrid system combing a floating wind platform and wave energy converters. *Appl. Energ.* **269**, 114998 (2020).
35. Zhang, D. et al. A coupled numerical framework for hybrid floating offshore wind turbine and oscillating water column wave energy converters. *Energ. Convers. Manage.* **267**, 115933 (2022).
36. Cong, P., Teng, B., Bai, W., Ning, D. & Liu, Y. Wave power absorption by an oscillating water column (OWC) device of annular cross-section in a combined wind-wave energy system. *Appl. Ocean. Res.* **107**, 102499 (2021).
37. Cheng, Y. et al. Wave energy extraction and hydroelastic response reduction of modular floating breakwaters as array wave energy converters integrated into a very large floating structure. *Appl. Energ.* **306**, 117953 (2022).
38. Nguyen, H. P. & Wang, C. M. Heaving wave energy converter-type attachments to a pontoon-type very large floating structure. *Eng. Struct.* **219**, 110964 (2020).
39. Nguyen, H. P. & Wang, C. M. Oscillating wave surge converter-type attachment for extracting wave energy while reducing hydroelastic responses of very large floating structures. *J. Offshore Mech. Arct.* **142** (4), 042001 (2020).
40. Nguyen, H. P., Wang, C. M. & Luong, V. H. Two-mode WEC-type attachment for wave energy extraction and reduction of hydroelastic response of pontoon-type VLFS. *Ocean. Eng.* **197**, 106875 (2020).
41. Tay, Z. Y. Performance and wave impact of an integrated multi-raft wave energy converter with floating breakwater for tropical climate. *Ocean. Eng.* **218**, 108136 (2020).
42. Zhang, H. et al. Hydrodynamic performance of a floating breakwater as an oscillating-buoy type wave energy converter. *Appl. energ.* **257**, 113996 (2020).
43. Cheng, Y. et al. Hydrodynamic characteristics of a hybrid oscillating water column-oscillating buoy wave energy converter integrated into a π-type floating breakwater. *Renew. Sust Energ. Rev.* **161**, 112299 (2022).
44. Cheng, Y. et al. Performance characteristics and parametric analysis of a novel multi-purpose platform combining a moonpool-type floating breakwater and an array of wave energy converters. *Appl. Energ.* **292**, 116888 (2021).
45. Yang, Y. et al. Performance and fatigue analysis of an integrated floating wind-current energy system considering the aero-hydro-servo-elastic coupling effects. *Renew. Energ.* **216**, 119111 (2023).
46. Yang, Y. et al. Effects of tidal turbine number on the performance of a 10 MW-class semi-submersible integrated floating wind-current system. *Energy* **285**, 128789 (2023).
47. Silva, R. N. et al. Dynamical analysis of a novel hybrid oceanic tidal-wave energy converter system. *Energy* **263**, 125933 (2023).
48. Du, X. et al. Dielectric elastomer wave energy harvester with self-bias voltage of an ancillary wind generator to power for intelligent buoys. *Energ. Convers. Manage.* **253**, 115178 (2022).
49. Du, X. et al. Vortex-induced piezoelectric cantilever beam vibration for ocean wave energy harvesting via airflow from the orifice of Oscillation water column chamber. *Nano Energy*. **104**, 107870 (2022).
50. Du, X., Zhang, M., Kang, H., Chang, H. & Yu, H. Theoretical study on a novel piezoelectric ocean wave energy harvester driven by oscillating water column. *Energ. Sour. Part A: Recov. Util.* **47**, 1–21 (2021).
51. Kumar, G. A. & Shivashankar Optimal power point tracking of solar and wind energy in a hybrid wind solar energy system. *Int. J. Energy Envir E.* **13** (1), 77–103 (2022).
52. Gangopadhyay, A., Seshadri, A. K., Sparks, N. J. & Toumi, R. The role of wind-solar hybrid plants in mitigating renewable energy-droughts. *Renew. Energ.* **194**, 926–937 (2022).
53. Liu, L. et al. Optimizing wind/solar combinations at finer scales to mitigate renewable energy variability in China. *Renew. Sust Energ. Rev.* **132**, 110151 (2020).
54. Jariwala, A. M., Dash, S. K., Sahu, U. K. & Chudjuarjeen, S. Design and dynamic emulation of hybrid solar-wind-wave energy converter (SWWEC) for efficient power generation. *Sci. Rep-UK*. **14** (1), 22721 (2024).
55. van der Zant, H. F. et al. The energy park of the future: Modelling the combination of wave-, wind-and solar energy in offshore multi-source parks. *Heliyon* https://doi.org/10.1016/j.heliyon.2024.e26788 (2024).
56. Shields, M., Beiter, P., Nunemaker, J., Cooperman, A. & Duffy, P. Impacts of turbine and plant upsizing on the levelized cost of energy for offshore wind. *Appl. Energ.* **298**, 117189 (2021).
57. Liu, S., Li, Q., Lu, B. & He, J. Impact of incoming turbulence intensity and turbine spacing on output power density: A study with two 5 MW offshore wind turbines. *Appl. Energ.* **371**, 123648 (2024).
58. ANSYS Inc. *ANSYS AQWA*. https://www.ansys.com/products/structures/ansys-aqwa (2018).
59. Bi, C. & Law, A. W. K. Co-locating offshore wind and floating solar farms–effect of high wind and wave conditions on solar power performance. *Energy* **266**, 126437 (2023).
60. Zhang, H., Cao, X. & Zhang, N. Hydrodynamic analysis of a novel box-type floating marine airport. *Ocean. Eng.* **298**, 117206 (2024).
61. Windt, C. et al. Validation of a CFD-based numerical wave tank model for the power production assessment of the wavestar ocean wave energy converter. *Renew. Energ.* **146**, 2499–2516 (2020).
62. Bredmose, H. et al. *Collation of Offshore wind-wave Dynamics Marine Renewables Infrastructure Network for Emerging Energy Technologies.* (2012).
63. Løken, I. B. & Kaynia, A. M. Effect of foundation type and modelling on dynamic response and fatigue of offshore wind turbines. *Wind Energy*. **22** (12), 1667–1683 (2019).
64. Jonkman, J., Butterfield, S., Musial, W. & Scott, G. *Definition of a 5-MW reference wind turbine for offshore system development (No. NREL/TP-500-38060).* (National Renewable Energy Lab. (NREL), 2009).
65. Kramer, M., Marquis, L. & Frigaard, P. Performance evaluation of the wavestar prototype. In: *9th ewtec 2011: Proceedings of the 9th European Wave and Tidal Conference.* (University of Southampton, 2011).

Acknowledgements
This research is supported by the National Research Foundation, Singapore, and PUB, Singapore's National Water Agency under its RIE2025 Urban Solutions and Sustainability (USS) (Water) Centre of Excellence (CoE) Programme which provides funding to the Nanyang Environment & Water Research Institute (NEWRI) of the Nanyang Technological University, Singapore (NTU). Any opinions, findings and conclusions or recommendations expressed in this material are those of the author(s) and do not reflect the views of National Research Foundation, Singapore and PUB, Singapore's National Water Agency. The financial support from the Department of Civil and Environmental Engineering, National University of Singapore, is also gratefully acknowledged.

Author contributions
Hongjian Zhang: Conceptualization, Methodology, Software, Validation, Formal analysis, Writing—Original draft preparation. Xiaodong Liu: Conceptualization, Validation, Writing—Review and Editing; Xinyu Cao: Validation, Investigation, Visualization; Ningchuan Zhang: Supervision, Data curation, Visualization; Adrian Wing-Keung Law: Conceptualization, Supervision, Formal analysis, Writing—Review and Editing.

Funding
This first author would like to acknowledge the support by the China Scholarship Council, China (NO.202306060117). The corresponding author gratefully acknowledges the financial support provided by the Department of Civil and Environmental Engineering, National University of Singapore.

Declarations

Competing interests
The authors declare no competing interests.

Additional information
Correspondence and requests for materials should be addressed to A.W.-K.L.